CHAPTER

8

INTEGRAL EQUATIONS, MOMENT METHOD, AND SELF AND MUTUAL IMPEDANCES

8.1 INTRODUCTION

In Chapter 2 it was shown, by the Thévenin and Norton equivalent circuits of Figures 2.21 and 2.22, that an antenna can be represented by an equivalent impedance $Z_A[Z_A = (R_r + R_L) + jX_A]$. The equivalent impedance is attached across two terminals (terminals $a - b$ in Figures 2.21 and 2.22) which are used to connect the antenna to a generator, receiver, or transmission line. In general, this impedance is called the *driving-point* impedance. However, when the antenna is radiating in an unbounded medium, in the absence of any other interfering elements or objects, the driving-point impedance is the same as the *self-impedance* of the antenna. In practice, however, there is always the ground whose presence must be taken into account in determining the antenna driving-point impedance. The self- and driving point impedances each have, in general, a real and an imaginary part. The real part is designated as the resistance and the imaginary part is called the reactance.

The impedance of an antenna depends on many factors including its frequency of operation, its geometry, its method of excitation, and its proximity to the surrounding objects. Because of their complex geometries, only a limited number of practical antennas have been investigated analytically. For many others, the input impedance has been determined experimentally.

The impedance of an antenna at a point is defined as the ratio of the electric to the magnetic fields at that point; alternatively, at a pair of terminals it is defined as the ratio of the voltage to the current across those terminals. There are many methods that can be used to calculate the impedance of an antenna [1]. Generally, these can be classified into three catogories: (1) the boundary-value method, (2) the transmission-line method, and (3) the Poynting vector method. Extensive and brief discussions and comparisons of these methods have been reported [1], [2].

The boundary-value approach is the most basic, and it treats the antenna as a boundary-value problem. The solution to this is obtained by enforcing the boundary

conditions (usually that the tangential electric field components vanish at the conducting surface). In turn, the current distribution and finally the impedance (ratio of applied emf to current) are determined, with no assumptions as to their distribution, as solutions to the problem. The principal disadvantage of this method is that it has limited applications. It can only be applied and solved exactly on simplified geometrical shapes where the scalar wave equation is separable.

The transmission-line method, which has been used extensively by Schelkunoff [3], treats the antenna as a transmission line, and it is most convenient for the biconical antenna. Since it utilizes tangential electric field boundary conditions for its solution, this technique may also be classified as a boundary-value method.

The basic approach to the Poynting vector method is to integrate the Poynting vector (power density) over a closed surface. The closed surface chosen is usually either a sphere of a very large radius r ($r \geq 2D^2/\lambda$ where D is the largest dimension of the antenna) or a surface that coincides with the surface of the antenna. The large sphere closed surface method has been introduced in Chapters 4 and 5, but it lends itself to calculations only of the real part of the antenna impedance (radiation resistance). The method that utilizes the antenna surface has been designated as the induced emf method, and it has been utilized [4]–[6] for the calculation of antenna impedances.

The impedance of an antenna can also be found using an integral equation with a numerical technique solution, which is widely referred to as the *Integral Equation-Method of Moments* [7]–[14]. This method, which in the late 1960s was extended to include electromagnetic problems, is analytically simple, it is versatile, but it requires large amounts of computation. The limitation of this technique is usually the speed and storage capacity of the computer.

In this chapter the integral equation method, with a Moment Method numerical solution, will be introduced and used first to find the self- and driving-point impedances, and mutual impedance of wire type of antennas. This method casts the solution for the induced current in the form of an integral (hence its name) where the unknown induced current density is part of the integrand. Numerical techniques, such as the *Moment Method* [7]–[14], can then be used to solve the current density. In particular two classical integral equations for linear elements, *Pocklington's and Hallén's Integral Equations*, will be introduced. This approach is very general, and it can be used with todays modern computational methods and equipment to compute the characteristics of complex configurations of antenna elements, including skewed arrangements. For special cases, closed form expressions for the self, driving point, and mutual impedances will be presented using the induced emf method. This method is limited to classical geometries, such as straight wires and arrays of collinear and parallel straight wires.

8.2 INTEGRAL EQUATION METHOD

The objective of the Integral Equation (IE) method for radiation or scattering is to cast the solution for the unknown current density, which is induced on the surface of the radiation scatterer, in the form of an integral equation where the unknown induced current density is part of the integrand. The integral equation is then solved for the unknown induced current density using numerical techniques such as the *Moment Method* (MM). To demonstrate this technique, we will initially consider some specific problems. For introduction, we will start with an electrostatics problem and follow it with time-harmonic problems.

8.2.1 Electrostatic Charge Distribution

In electrostatics, the problem of finding the potential that is due to a given charge distribution is often considered. In physical situations, however, it is seldom possible to specify a charge distribution. Whereas we may connect a conducting body to a voltage source, and thus specify the potential throughout the body, the distribution of charge is obvious only for a few rotationally symmetric geometries. In this section we will consider an integral equation approach to solve for the electric charge distribution once the electric potential is specified. Some of the material here and in other sections is drawn from [15], [16].

From statics we know that a linear electric charge distribution $\rho(r')$ creates an electric potential, $V(r)$, according to [17]

$$V(r) = \frac{1}{4\pi\epsilon_0} \int_{\substack{\text{source} \\ \text{(charge)}}} \frac{\rho(r')}{R}\, dl' \tag{8-1}$$

where $r'(x', y', z')$ denotes the source coordinates, $r(x, y, z)$ denotes the observation coordinates, dl' is the path of integration, and R is the distance from any one point on the source to the observation point, which is generally represented by

$$R(r, r') = |\mathbf{r} - \mathbf{r}'| = \sqrt{(x - x')^2 + (y - y')^2 + (z - z')^2} \tag{8-1a}$$

We see that (8-1) may be used to calculate the potentials that are due to any known line charge density. However, the charge distribution on most configurations of practical interest, i.e., complex geometries, is not usually known, even when the potential on the source is given. It is the nontrivial problem of determining the charge distribution, for a specified potential, that is to be solved here using an integral equation-numerial solution approach.

A. Finite Straight Wire

Consider a straight wire of length l and radius a, placed along the y axis, as shown in Figure 8-1(a). The wire is given a normalized constant electric potential of 1 V.

Note that (8-1) is valid everywhere, including on the wire itself ($V_{\text{wire}} = 1$ V). Thus, choosing the observation along the wire axis ($x = z = 0$) and representing the charge density on the surface of the wire, (8-1) can be expressed as

$$1 = \frac{1}{4\pi\epsilon_0} \int_0^l \frac{\rho(y')}{R(y, y')}\, dy', \quad 0 \le y \le l \tag{8-2}$$

where

$$R(y, y') = R(r, r')|_{x=z=0} = \sqrt{(y - y')^2 + |(x')^2 + (z')^2|}$$

$$= \sqrt{(y - y')^2 + a^2} \tag{8-2a}$$

The observation point is chosen along the wire axis and the charge density is represented along the surface of the wire to avoid $R(y, y') = 0$, which would introduce a singularity in the integrand of (8-2).

It is necessary to solve (8-2) for the unknown $\rho(y')$ (an inversion problem). Equation (8-2) is an integral equation that can be used to find the charge density $\rho(y')$ based on the 1-V potential. The solution may be reached numerically by reducing (8-2) to a series of linear algebraic equations that may be solved by conventional matrix equation techniques. To facilitate this, let us approximate the unknown charge

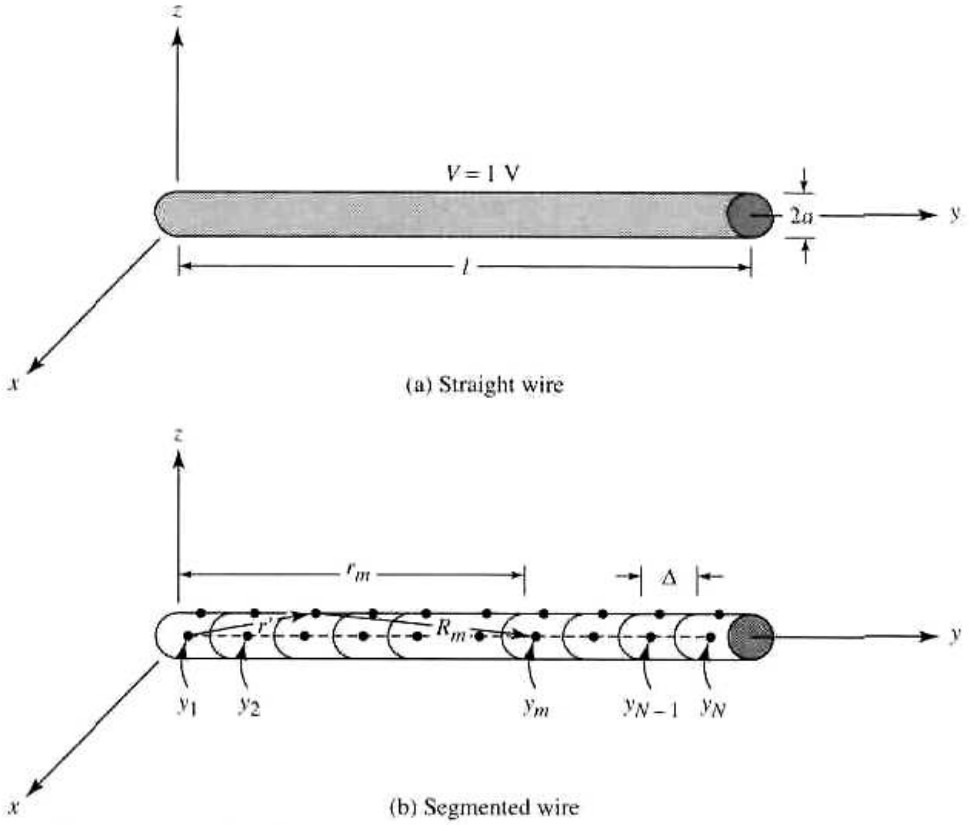

Figure 8.1 Straight wire of constant potential and its segmentation.

distribution $\rho(y')$ by an expansion of N known terms with constant, but unknown, coefficients, that is,

$$\rho(y') = \sum_{n=1}^{N} a_n g_n(y') \tag{8-3}$$

Thus, (8-2) may be written, using (8-3), as

$$4\pi\epsilon_0 = \int_0^l \frac{1}{R(y, y')} \left[\sum_{n=1}^{N} a_n g_n(y') \right] dy' \tag{8-4}$$

Because (8-4) is a nonsingular integral, its integration and summation can be interchanged, and it can be written as

$$4\pi\epsilon_0 = \sum_{n=1}^{N} a_n \int_0^l \frac{g_n(y')}{\sqrt{(y - y')^2 + a^2}} dy' \tag{8-4a}$$

The wire is now divided into N uniform segments, each of length $\Delta = l/N$, as illustrated in Figure 8.1(b). The $g_n(y')$ functions in the expansion (8-3) are chosen for their ability to accurately model the unknown quantity, while minimizing computation. They are often referred to as *basis* (or expansion) functions, and they will be discussed further in Section 8.2.3. To avoid complexity in this solution, subdomain piecewise constant (or "pulse") functions will be used. These functions, shown in Figure 8.5, are defined to be of a constant value over one segment and zero elsewhere, or

$$g_n(y') = \begin{cases} 0 & y' < (n-1)\Delta \\ 1 & (n-1)\Delta \le y' \le n\Delta \\ 0 & n\Delta < y' \end{cases} \tag{8-5}$$

Many other basis functions are possible, some of which will be introduced later in *Section 8.2.3.*

Replacing y in (8-4) by a fixed point such as y_m, results in an integrand that is solely a function of y', so the integral may be evaluated. Obviously, (8-4) leads to one equation with N unknowns a_n written as

$$\begin{aligned} 4\pi\epsilon_0 = a_1 \int_0^{\Delta} \frac{g_1(y')}{R(y_m, y')} dy' + a_2 \int_{\Delta}^{2\Delta} \frac{g_2(y')}{R(y_m, y')} dy' + \cdots \\ + a_n \int_{(n-1)\Delta}^{n\Delta} \frac{g_n(y')}{R(y_m, y')} dy' + \cdots + a_N \int_{(N-1)\Delta}^{l} \frac{g_N(y')}{R(y_m, y')} dy' \end{aligned} \tag{8-6}$$

In order to obtain a solution for these N amplitude constants, N linearly independent equations are necessary. These equations may be produced by choosing N observation points y_m each at the center of each Δ length element as shown in Figure 8.1(b). This results in one equation of the form of (8-6) corresponding to each observation point. For N such points, we can reduce (8-6) to

$$\begin{aligned} 4\pi\epsilon_0 &= a_1 \int_0^{\Delta} \frac{g_1(y')}{R(y_1, y')} dy' + \cdots + a_N \int_{(N-1)\Delta}^{l} \frac{g_N(y')}{R(y_1, y')} dy' \\ &\vdots \\ 4\pi\epsilon_0 &= a_1 \int_0^{\Delta} \frac{g_1(y')}{R(y_N, y')} dy' + \cdots + a_N \int_{(N-1)\Delta}^{l} \frac{g_N(y')}{R(y_N, y')} dy' \end{aligned} \tag{8-6a}$$

We may write (8-6a) more concisely using matrix notation as

$$[V_m] = [Z_{mn}][I_n] \tag{8-7}$$

where each Z_{mn} term is equal to

$$\begin{aligned} Z_{mn} &= \int_0^{l} \frac{g_n(y')}{\sqrt{(y_m - y')^2 + a^2}} dy' \\ &= \int_{(n-1)\Delta}^{n\Delta} \frac{1}{\sqrt{(y_m - y')^2 + a^2}} dy' \end{aligned} \tag{8-7a}$$

and

$$[I_n] = [a_n] \tag{8-7b}$$

$$[V_m] = [4\pi\epsilon_0]. \tag{8-7c}$$

The V_m column matrix has all terms equal to $4\pi\epsilon_0$, and the $I_n = a_n$ values are the unknown charge distribution coefficients. Solving (8-7) for $[I_n]$ gives

$$[I_n] = [a_n] = [Z_{mn}]^{-1}[V_m] \tag{8-8}$$

Either (8-7) or (8-8) may readily be solved on a digital computer by using any of a number of matrix inversion or equation solving routines. Whereas the integral involved here may be evaluated in closed form by making appropriate approximations, this is not usually possible with more complicated problems. Efficient numerical integral computer subroutines are commonly available in easy-to-use forms.

One closed form evaluation of (8-7a) is to reduce the integral and represent it by

$$Z_{mn} = \begin{cases} 2 \ln\left(\dfrac{\dfrac{\Delta}{2} + \sqrt{a^2 + \left(\dfrac{\Delta}{2}\right)^2}}{a}\right) & m = n \quad (8\text{-}9a) \\ \ln\left\{\dfrac{d_{mn}^{+} + [(d_{mn}^{+})^2 + a^2]^{1/2}}{d_{mn}^{-} + [(d_{mn}^{-})^2 + a^2]^{1/2}}\right\} & m \neq n \text{ but } |m - n| \leq 2 \quad (8\text{-}9b) \\ \ln\left(\dfrac{d_{mn}^{+}}{d_{mn}^{-}}\right) & |m - n| > 2 \quad (8\text{-}9c) \end{cases}$$

where

$$d_{mn}^{+} = l_m + \frac{\Delta}{2} \quad (8\text{-}9d)$$

$$d_{mn}^{-} = l_m - \frac{\Delta}{2} \quad (8\text{-}9e)$$

l_m is the distance between the mth matching point and the center of the nth source point.

In summary, the solution of (8-2) for the charge distribution on a wire has been accomplished by approximating the unknown with some basis functions, dividing the wire into segments, and then sequentially enforcing (8-2) at the center of each segment to form a set of linear equations.

Even for the relatively simple straight wire geometry we have discussed, the exact form of the charge distribution is not intuitively apparent. To illustrate the principles of the numerical solution, an example is now presented.

Example 8.1

A 1-m long straight wire of radius $a = 0.001$ m is maintained at a constant potential of 1 V. Determine the linear charge distribution on the wire by dividing the length into 5 and 20 uniform segments. Assume subdomain pulse basis functions.

SOLUTION

1. $N = 5$. When the 1-m long wire is divided into five uniform segments each of length $\Delta = 0.2$ m, (8-7) reduces to

$$\begin{bmatrix} 10.60 & 1.10 & 0.51 & 0.34 & 0.25 \\ 1.10 & 10.60 & 1.10 & 0.51 & 0.34 \\ 0.51 & 1.10 & 10.60 & 1.10 & 0.51 \\ 0.34 & 0.51 & 1.10 & 10.60 & 1.10 \\ 0.25 & 0.34 & 0.51 & 1.10 & 10.60 \end{bmatrix} \begin{bmatrix} a_1 \\ a_2 \\ a_3 \\ a_4 \\ a_5 \end{bmatrix} = \begin{bmatrix} 1.11 \times 10^{-10} \\ 1.11 \times 10^{-10} \\ \vdots \\ 1.11 \times 10^{-10} \end{bmatrix}$$

Inverting this matrix leads to the amplitude coefficients and subsequent charge distribution of

$$a_1 = 8.81 pC/m$$

$$a_2 = 8.09 pC/m$$

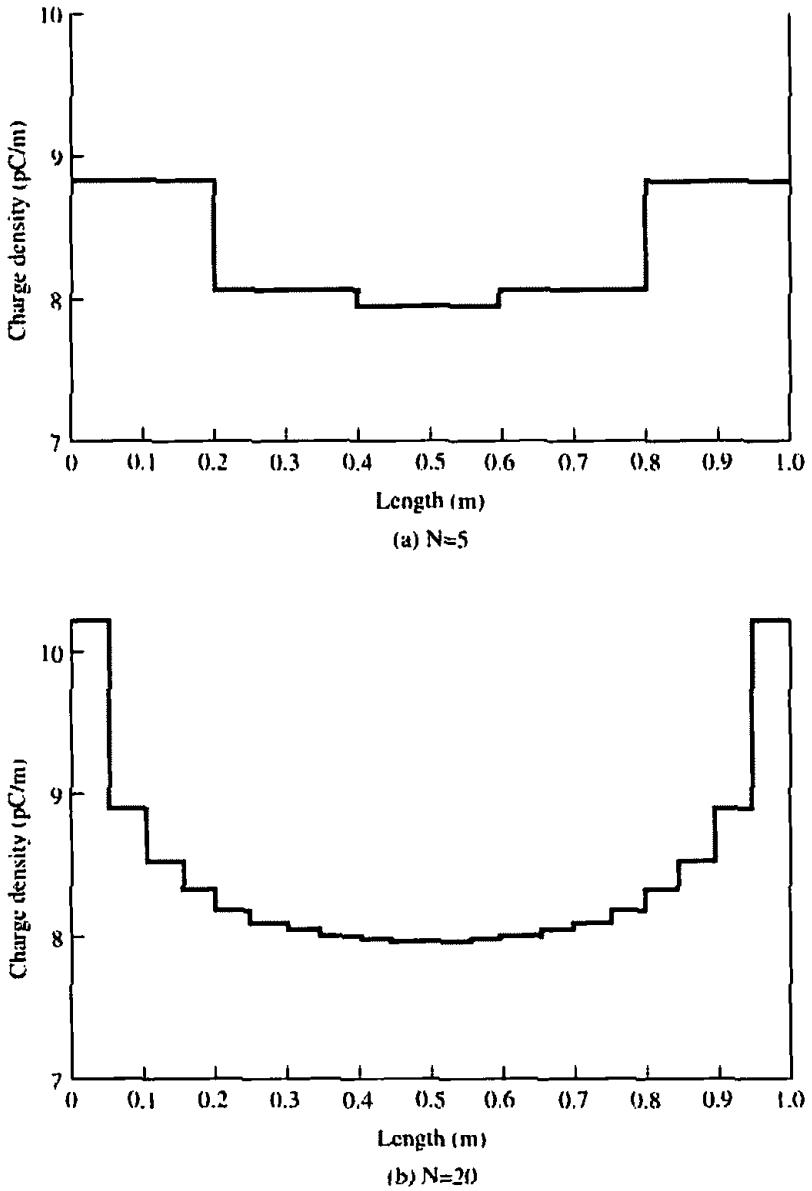

Figure 8.2 Charge distribution on a 1-m straight wire at 1 V.

$$a_3 = 7.97 pC/m$$
$$a_4 = 8.09 pC/m$$
$$a_5 = 8.81 pC/m$$

The charge distribution is shown in Figure 8.2(a).

2. $N = 20$. Increasing the number of segments to 20 results in a much smoother distribution, as shown plotted in Figure 8.2(b). As more segments are used, a better approximation of the actual charge distribution is attained, which has smaller discontinuities over the length of the wire.

B. Bent Wire

In order to illustrate the solution of a more complex structure, let us analyze a body composed of two noncollinear straight wires; that is, a bent wire. If a straight wire is bent, the charge distribution will be altered, although the solution to find it will differ

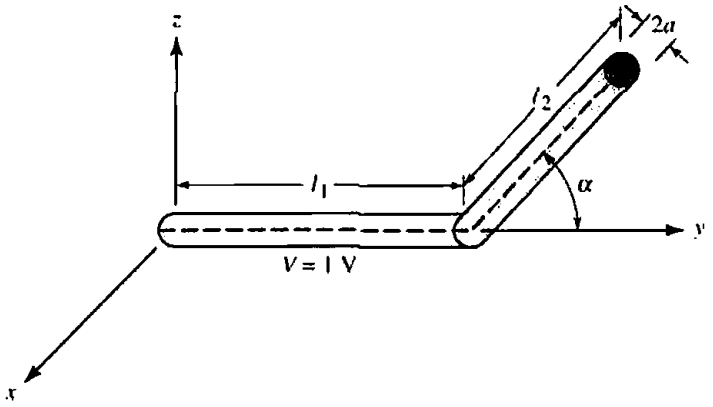

Figure 8.3 Geometry for bent wire.

only slightly from the straight wire case. We will assume a bend of angle α, which remains on the yz-plane, as shown in Figure 8.3.

For the first segment l_1 of the wire, the distance R can be represented by (8-2a). However, for the second segment l_2 we can express the distance as

$$R = \sqrt{(y - y')^2 + (z - z')^2} \tag{8-10}$$

Also because of the bend, the integral in (8-7a) must be separated into two parts of

$$Z_{mn} = \int_0^{l_1} \frac{\rho_n(l_1')}{R} dl_1' + \int_0^{l_2} \frac{\rho_n(l_2')}{R} dl_2' \tag{8-11}$$

where l_1 and l_2 are measured along the corresponding straight sections from their left ends.

Example 8.2

Repeat Example 8.1 assuming that the wire has been bent 90° at its midpoint. Subdivide the wire into 20 uniform segments.

SOLUTION

The charge distribution for this case, calculated using (8-10) and (8-11), is plotted in Figure 8.4 for $N = 20$ segments. Note that the charge is relatively more concentrated near the ends of this structure than was the case for a straight wire of Figure 8.2(b). Further, the overall density, and thus capacitance, on the structure has decreased.

Arbitrary wire configurations, including numerous ends and even curved sections, may be analyzed by the methods already outlined here. As with the simple bent wire, the only alterations generally necessary are those required to describe the geometry analytically.

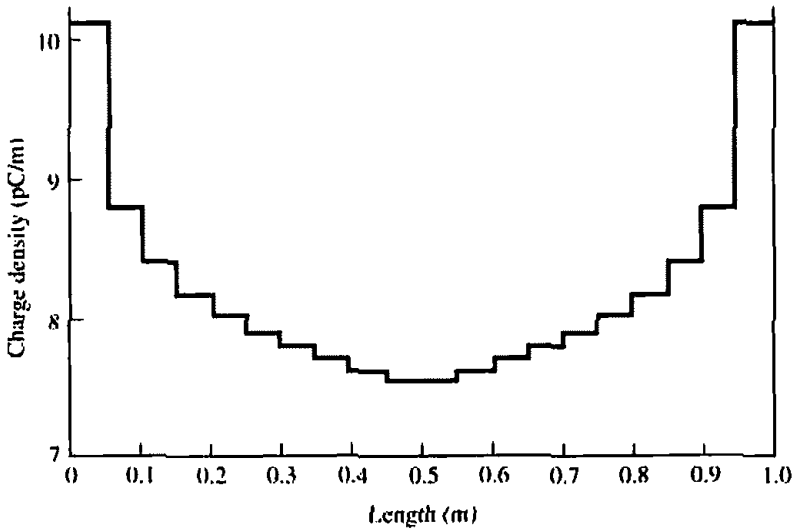

Figure 8.4 Charge distribution on a 1-m bent wire ($\alpha = 90°$, $N = 20$).

8.2.2 Integral Equation

Equation (8-2) for the 1-V potential on a wire of length l is an integral equation, which can be used to solve for the charge distribution. Numerically this is accomplished using a method, which is usually referred to as *Moment Method* or *Method of Moments* [7]–[14]. To solve (8-2) numerically the unknown charge density $\rho(y')$ is represented by N terms, as given by (8-3). In (8-3) $g_n(y')$ are a set of N known functions, usually referred to as *basis* or *expansion* functions, while a_n represents a set of N constant, but unknown, coefficients. The basis or expansion functions are chosen to best represent the unknown charge distribution.

Equation (8-2) is valid at every point on the wire. By enforcing (8-2) at N discrete but different points on the wire, the integral equation of (8-2) is reduced to a set of N linearly independent algebraic equations, as given by (8-6a). This set is generalized by (8-7)–(8-7c), which is solved for the unknown coefficients a_n by (8-8) using matrix inversion techniques. Since the system of N linear equations each with N unknowns, as given by (8-6a)–(8-8), was derived by applying the boundary condition (constant 1-V potential) at N discrete points on the wire, the technique is referred to as *point-matching* (or *collocation*) method [7], [8]. Thus, by finding the elements of the $[V]$ and $[Z]$, and then the inverse $[Z]^{-1}$ matrices, we can then determine the coefficients a_n of the $[I]$ matrix using (8-8). This in turn allows us to approximate the charge distribution $\rho(y')$ using (8-3). This was demonstrated by Examples 8.1 and 8.2 for the straight and bent wires, respectively.

In general, there are many forms of integral equations. For time-harmonic electromagnetics, two of the most popular integral equations are the *electric field integral equation* (EFIE) and the *magnetic field integral equation* (MFIE) [14]. The EFIE enforces the boundary condition on the tangential electric field while the MFIE enforces the boundary condition on the tangential components of the magnetic field. The EFIE is valid for both closed or open surfaces while the MFIE is valid for closed surfaces. These integral equations can be used for both radiation and scattering problems. Two- and three-dimensional EFIE and MFIE equations for TE and TM polarizations are derived and demonstrated in [14]. For radiation problems, especially wire antennas, two popular EFIEs are the Pocklington Integral Equation and the Hallén

Integral Equation. Both of these will be discussed and demonstrated in the section that follows.

8.3 FINITE DIAMETER WIRES

In this section we want to derive and apply two classic three-dimensional integral equations, referred to as *Pocklington's integrodifferential equation* and *Hallén's integral equation* [18]–[26], that can be used most conveniently to find the current distribution on conducting wires. Hallén's equation is usually restricted to the use of a *delta-gap* voltage source model at the feed of a wire antenna. Pocklington's equation, however, is more general and it is adaptable to many types of feed sources (through alteration of its excitation function or excitation matrix), including a magnetic frill [27]. In addition, Hallén's equation requires the inversion of an $N + 1$ order matrix (where N is the number of divisions of the wire) while Pocklington's equation requires the inversion of an N order matrix.

For very thin wires, the current distribution is usually assumed to be of sinusoidal form as given by (4-56). For finite diameter wires (usually diameters d of $d > 0.05\lambda$), the sinusoidal current distribution is representative but not accurate. To find a more accurate current distribution on a cylindrical wire, an integral equation is usually derived and solved. Previously, solutions to the integral equation were obtained using iterative methods [20]; presently, it is most convenient to use moment method techniques [7]–[9].

If we know the voltage at the feed terminals of a wire antenna and find the current distribution, the input impedance and radiation pattern can then be obtained. Similarly, if a wave impinges upon the surface of a wire scatterer, it induces a current density that in turn is used to find the scattered field. Whereas the linear wire is simple, most of the information presented here can be readily extended to more complicated structures.

8.3.1 Pocklington's Integral Equation

To derive Pocklington's integral equation, refer to Figure 8.5. Although this derivation is general, it can be used either when the wire is a scatterer or an antenna. Let us assume that an incident wave impinges on the surface of a conducting wire, as shown in Figure 8.5(a), and it is referred to as the *incident electric field* $\mathbf{E}^i(\mathbf{r})$. When the wire is an antenna, the incident field is produced by the feed at the gap, as shown in Figure 8.7. Part of the incident field impinges on the wire and induces on its surface a linear current density $\mathbf{J}_s$ (amperes per meter). The induced current density $\mathbf{J}_s$ reradiates and produces an electric field that is referred to as the *scattered electric field* $\mathbf{E}^s(\mathbf{r})$. Therefore, at any point in space the total electric field $\mathbf{E}^t(\mathbf{r})$ is the sum of the incident and scattered fields, or

$$\mathbf{E}^t(\mathbf{r}) = \mathbf{E}^i(\mathbf{r}) + \mathbf{E}^s(\mathbf{r}) \tag{8-12}$$

where

$\mathbf{E}^t(\mathbf{r})$ = total electric field

$\mathbf{E}^i(\mathbf{r})$ = incident electric field

$\mathbf{E}^s(\mathbf{r})$ = scattered electric field

When the observation point is moved to the surface of the wire ($r = r_s$) and the wire is perfectly conducting, the total tangential electric field vanishes. In cylindrical

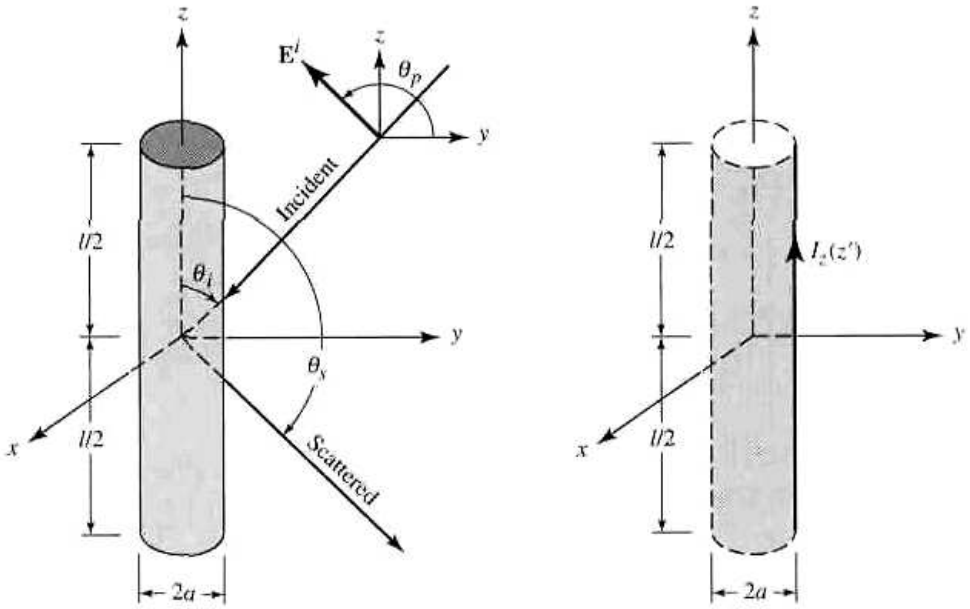

(a) Geometry (b) Equivalent current

Figure 8.5 Uniform plane wave obliquely incident on a conducting wire.

coordinates, the electric field radiated by the dipole has a radial component (E_ρ) and a tangential component (E_z). These are represented by (8-55a) and (8-55b). Therefore on the surface of the wire the tangential component of (8-12) reduces to

$$E_z^t(r = r_s) = E_z^i(r = r_s) + E_z^s(r = r_s) = 0 \tag{8-13}$$

or

$$E_z^s(r = r_s) = -E_z^i(r = r_s) \tag{8-13a}$$

In general, the scattered electric field generated by the induced current density $\mathbf{J}_s$ is given by (3-15), or

$$\begin{aligned} \mathbf{E}^s(\mathbf{r}) &= -j\omega\mathbf{A} - j\frac{1}{\omega\mu\epsilon}\nabla(\nabla\cdot\mathbf{A}) \\ &= -j\frac{1}{\omega\mu\epsilon}[k^2\,\mathbf{A} + \nabla(\nabla\cdot\mathbf{A})] \end{aligned} \tag{8-14}$$

However, for observations at the wire surface only the z component of (8-14) is needed, and we can write it as

$$E_z^s(r) = -j\frac{1}{\omega\mu\epsilon}\left(k^2 A_z + \frac{\partial^2 A_z}{\partial z^2}\right) \tag{8-15}$$

According to (3-51) and neglecting edge effects

$$A_z = \frac{\mu}{4\pi}\iint_S J_z\frac{e^{-jkR}}{R}\,ds' = \frac{\mu}{4\pi}\int_{-l/2}^{+l/2}\int_0^{2\pi} J_z\frac{e^{-jkR}}{R}\,a\,d\phi'\,dz' \tag{8-16}$$

If the wire is very thin, the current density J_z is not a function of the azimuthal angle ϕ, and we can write it as

$$2\pi a J_z = I_z(z') \Rightarrow J_z = \frac{1}{2\pi a}I_z(z') \tag{8-17}$$

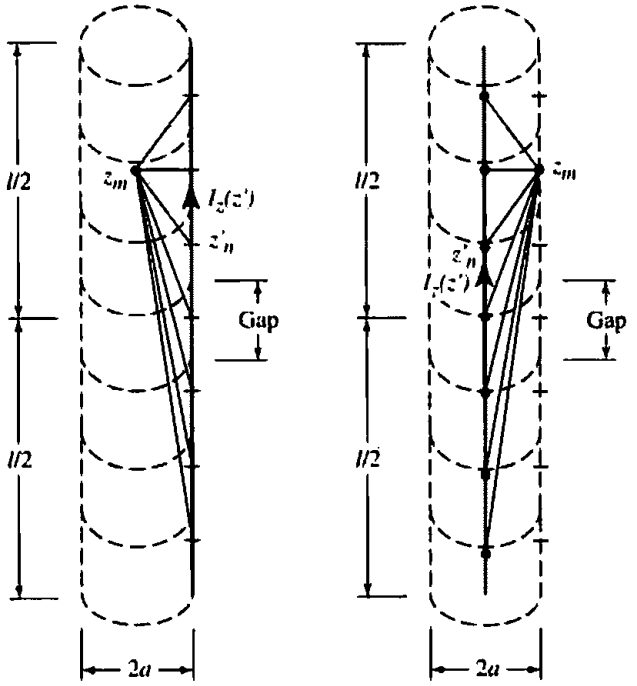

(a) On the surface (b) Along the center

Figure 8.6 Dipole segmentation and its equivalent current.

where $I_z(z')$ is assumed to be an equivalent filament line-source current located a radial distance $\rho = a$ from the z axis, as shown in Figure 8.6(a). Thus (8-16) reduces to

$$A_z = \frac{\mu}{4\pi}\int_{-l/2}^{+l/2}\left[\frac{1}{2\pi a}\int_0^{2\pi} I_z(z')\frac{e^{-jkR}}{R}a\,d\phi'\right]dz' \tag{8-18}$$

$$\begin{aligned} R &= \sqrt{(x-x')^2 + (y-y')^2 + (z-z')^2} \\ &= \sqrt{(\rho^2 + a^2 - 2\rho a\cos(\phi-\phi') + (z-z')^2} \end{aligned} \tag{8-18a}$$

where ρ is the radial distance to the observation point and a is the radius.

Because of the symmetry of the scatterer, the observations are not a function of ϕ. For simplicity, let us then choose $\phi = 0$. For observations on the surface $\rho = a$ of the scatterer (8-18) and (8-18a) reduce to

$$\begin{aligned} A_z(\rho = a) &= \mu\int_{-l/2}^{+l/2} I_z(z')\left(\frac{1}{2\pi}\int_0^{2\pi}\frac{e^{-jkR}}{4\pi R}d\phi'\right)dz' \\ &= \mu\int_{-l/2}^{+l/2} I_z(z')G(z,z')\,dz' \end{aligned} \tag{8-19}$$

$$G(z,z') = \frac{1}{2\pi}\int_0^{2\pi}\frac{e^{-jkR}}{4\pi R}d\phi' \tag{8-19a}$$

$$R(\rho = a) = \sqrt{4a^2\sin^2\left(\frac{\phi'}{2}\right) + (z-z')^2} \tag{8-19b}$$

Thus for observations at the surface $\rho = a$ of the scatterer, the z component of the scattered electric field can be expressed as

$$E_z^s(\rho = a) = -j\frac{1}{\omega\epsilon}\left(k^2 + \frac{d^2}{dz^2}\right)\int_{-l/2}^{+l/2} I_z(z')G(z, z')\,dz' \tag{8-20}$$

which by using (8-13a) reduces to

$$-j\frac{1}{\omega\epsilon}\left(\frac{d^2}{dz^2} + k^2\right)\int_{-l/2}^{+l/2} I_z(z')G(z, z')\,dz' = -E_z^i(\rho = a) \tag{8-21}$$

or

$$\left(\frac{d^2}{dz^2} + k^2\right)\int_{-l/2}^{+l/2} I_z(z')G(z, z')\,dz' = -j\omega\epsilon E_z^i(\rho = a) \tag{8-21a}$$

Interchanging integration with differentiation, we can rewrite (8-21a) as

$$\int_{-l/2}^{+l/2} I_z(z')\left[\left(\frac{\partial^2}{\partial z^2} + k^2\right)G(z, z')\right]dz' = -j\omega\epsilon E_z^i(\rho = a) \tag{8-22}$$

where $G(z, z')$ is given by (8-19a).

Equation (8-22) is referred to as *Pocklington's integral equation* [1], and it can be used to determine the equivalent filamentary line-source current of the wire, and thus current density on the wire, by knowing the incident field on the surface of the wire.

If we assume that the wire is very thin ($a \ll \lambda$) such that (8-19a) reduces to

$$G(z, z') = G(R) = \frac{e^{-jkR}}{4\pi R} \tag{8-23}$$

(8-22) can also be expressed in a more convenient form as [22]

$$\int_{-l/2}^{+l/2} I_z(z')\frac{e^{-jkR}}{4\pi R^5}[(1 + jkR)(2R^2 - 3a^2) + (kaR)^2]\,dz' = -j\omega\epsilon E_z^i(\rho = a) \tag{8-24}$$

where for observations along the center of the wire ($\rho = 0$)

$$R = \sqrt{a^2 + (z - z')^2} \tag{8-24a}$$

In (8-22) or (8-24), $I_z(z')$ represents the equivalent filamentary line-source current located on the surface of the wire, as shown in Figure 8.5(b), and it is obtained by knowing the incident electric field on the surface of the wire. By point-matching techniques, this is solved by matching the boundary conditions at discrete points on the surface of the wire. Often it is easier to choose the matching points to be at the interior of the wire, especially along the axis as shown in Figure 8.6(a), where $I_z(z')$ is located on the surface of the wire. By reciprocity, the configuration of Figure 8.6(a) is analogous to that of Figure 8.6(b) where the equivalent filamentary line-source current is assumed to be located along the center axis of the wire and the matching points are selected on the surface of the wire. Either of the two configurations can be used to determine the equivalent filamentary line-source current $I_z(z')$; the choice is left to the individual.

8.3.2 Hallén's Integral Equation

Referring again to Figure 8.5(a), let us assume that the length of the cylinder is much larger than its radius ($l \gg a$) and its radius is much smaller than the wavelength ($a \ll \lambda$) so that the effects of the end faces of the cylinder can be neglected. Therefore the boundary conditions for a wire with infinite conductivity are those of vanishing total tangential **E** fields on the surface of the cylinder and vanishing current at the ends of the cylinder [$I_z(z' = \pm l/2) = 0$].

Since only an electric current density flows on the cylinder and it is directed along the z axis ($\mathbf{J} = \hat{\mathbf{a}}_z J_z$), then according to (3-14) and (3-51) $\mathbf{A} = \hat{\mathbf{a}}_z A_z(z')$, which for small radii is assumed to be only a function of z'. Thus (3-15) reduces to

$$E_z^i = -j\omega A_z - j\frac{1}{\omega\mu\epsilon}\frac{\partial^2 A_z}{\partial z^2} = -j\frac{1}{\omega\mu\epsilon}\left[\frac{d^2 A_z}{dz^2} + \omega^2\mu\epsilon A_z\right] \tag{8-25}$$

Since the total tangential electric field E_z^i vanishes on the surface of the cylinder, (8-25) reduces to

$$\frac{d^2 A_z}{dz^2} + k^2 A_z = 0 \tag{8-25a}$$

Because the current density on the cylinder is symmetrical [$J_z(z') = J_z(-z')$], the potential A_z is also symmetrical (i.e., $A_z(z') = A_z(-z')$]. Thus the solution of (8-25a) is given by

$$A_z(z) = -j\sqrt{\mu\epsilon}[B_1 \cos(kz) + C_1 \sin(k|z|)] \tag{8-26}$$

where B_1 and C_1 are constants. For a current-carrying wire, its potential is also given by (3-53). Equating (8-26) to (3-53) leads to

$$\int_{-l/2}^{+l/2} I_z(z')\frac{e^{-jkR}}{4\pi R}dz' = -j\sqrt{\frac{\epsilon}{\mu}}[B_1 \cos(kz) + C_1 \sin(k|z|)] \tag{8-27}$$

If a voltage V_i is applied at the input terminals of the wire, it can be shown that the constant $C_1 = V_i/2$. The constant B_1 is determined from the boundary condition that requires the current to vanish at the end points of the wire.

Equation (8-27) is referred to as *Hallén's integral equation* for a perfectly conducting wire. It was derived by solving the differential equation (3-15) or (8-25a) with the enforcement of the appropriate boundary conditions.

8.3.3 Source Modeling

Let us assume that the wire of Figure 8.5 is symmetrically fed by a voltage source, as shown in Figure 8.7(a), and the element acting as a dipole antenna. To use, for example, Pocklington's integrodifferential equation (8-22) or (8-23) we need to know how to express $E_z^i(\rho = a)$. Traditionally there have been two methods used to model the excitation to represent $E_z^i(\rho = a, 0 \le \phi \le 2\pi, -l/2 \le z \le +l/2)$ at all points on the surface of the dipole: One is referred to as the *delta-gap* excitation and the other as the *equivalent magnetic ring current* (better known as *magnetic frill generator*) [27].

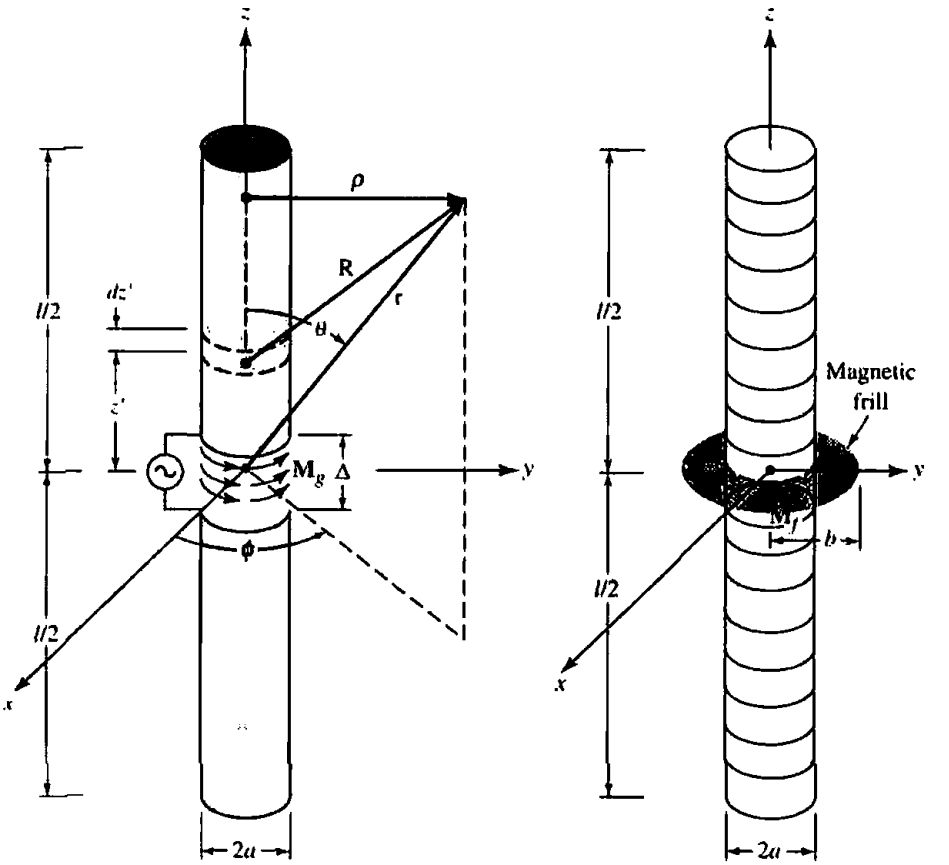

Figure 8.7 Cylindrical dipole, its segmentation, and gap modeling.

A. Delta Gap

The delta-gap source modeling is the simplest and most widely used of the two, but it is also the least accurate, especially for impedances. Usually it is most accurate for smaller width gaps. Using the delta gap, it is assumed that the excitation voltage at the feed terminals is of a constant V_i value and zero elsewhere. Therefore the incident electric field $E_z^i(\rho = a,\ 0 \le \phi \le 2\pi,\ -l/2 \le z \le +l/2)$ is also a constant (V_i/Δ where Δ is the gap width) over the feed gap and zero elsewhere, hence the name delta gap. For the delta-gap model, the feed gap Δ of Figure 8.7(a) is replaced by a narrow band of strips of equivalent magnetic current density of

$$\mathbf{M}_g = -\hat{\mathbf{n}} \times \mathbf{E}^i = -\hat{\mathbf{a}}_\rho \times \hat{\mathbf{a}}_z \frac{V_i}{\Delta} = \hat{\mathbf{a}}_\phi \frac{V_i}{\Delta} \qquad -\frac{\Delta}{2} \le z' \le \frac{\Delta}{2} \tag{8-28}$$

The magnetic current density $\mathbf{M}_g$ is sketched in Figure 8.7(a).

B. Magnetic Frill Generator

The magnetic frill generator was introduced to calculate the near- as well as the far-zone fields from coaxial apertures [27]. To use this model, the feed gap is replaced with a circumferentially directed magnetic current density that exists over an annular aperture with inner radius a, which is usually chosen to be the radius of the wire, and an outer radius b, as shown in Figure 8.7(b). Since the dipole is usually fed by transmission lines, the outer radius b of the equivalent annular aperture of the magnetic frill generator is found using the expression for the characteristic impedance of the transmission line.

Over the annular aperture of the magnetic frill generator, the electric field is represented by the TEM mode field distribution of a coaxial transmission line given by

$$\mathbf{E}_f = \hat{\mathbf{a}}_\rho \frac{V_i}{2\rho' \ln(b/a)} \quad a \le \rho' \le b \tag{8-29}$$

Therefore the corresponding equivalent magnetic current density $\mathbf{M}_f$ for the magnetic frill generator used to represent the aperture is equal to

$$\mathbf{M}_f = -2\hat{\mathbf{n}} \times \mathbf{E}_f = -2\hat{\mathbf{a}}_z \times \hat{\mathbf{a}}_\rho E_\rho = -\hat{\mathbf{a}}_\phi \frac{V_i}{\rho' \ln(b/a)} \quad a \le \rho' \le b \tag{8-30}$$

The fields generated by the magnetic frill generator of (8-30) on the surface of the wire are found by using [27]

$$\begin{aligned} E_z^i\left(\rho = a, 0 \le \phi \le 2\pi, -\frac{l}{2} \le z \le \frac{l}{2}\right) &\simeq -V_i\left(\frac{k(b^2 - a^2)e^{-jkR_0}}{8\ln(b/a)R_0^2}\left\{2\left[\frac{1}{kR_0} + j\left(1 - \frac{b^2 - a^2}{2R_0^2}\right)\right]\right.\right. \\ &+ \frac{a^2}{R_0}\left[\left(\frac{1}{kR_0} + j\left(1 - \frac{(b^2 + a^2)}{2R_0^2}\right)\right)\left(-jk - \frac{2}{R_0}\right)\right. \\ &\left.\left.\left. + \left(-\frac{1}{kR_0^2} + j\frac{b^2 + a^2}{R_0^3}\right)\right]\right\}\right) \end{aligned} \tag{8-31}$$

where

$$R_0 = \sqrt{z^2 + a^2} \tag{8-31a}$$

The fields generated on the surface of the wire computed using (8-31) can be approximated by those found along the axis ($\rho = 0$). Doing this leads to a simpler expression of the form [27]

$$E_z^i\left(\rho = 0, -\frac{l}{2} \le z \le \frac{l}{2}\right) = -\frac{V_i}{2\ln(b/a)}\left[\frac{e^{-jkR_1}}{R_1} - \frac{e^{-jkR_2}}{R_2}\right] \tag{8-32}$$

where

$$R_1 = \sqrt{z^2 + a^2} \tag{8-32a}$$

$$R_2 = \sqrt{z^2 + b^2} \tag{8-32b}$$

To compare the results using the two source modelings (delta-gap and magnetic-frill generator), an example is performed.

Example 8.3

For a center-fed linear dipole of $l = 0.47\lambda$ and $a = 0.005\lambda$, determine the induced voltage along the length of the dipole based on the incident electric field of the magnetic frill of (8-32). Subdivide the wire into 21 segments ($N = 21$). Compare the induced voltage distribution based on the magnetic frill to that of the delta gap. Assume a 50-ohm characteristic impedance with free space between the conductors for the annular feed.

SOLUTION

Since the characteristic impedance of the annular aperture is 50 ohms, then

$$Z_c = \sqrt{\frac{\mu_0}{\epsilon_0}}\frac{\ln(b/a)}{2\pi} = 50 \quad \Rightarrow \quad \frac{b}{a} = 2.3$$

Subdividing the total length ($l = 0.47\lambda$) of the dipole to 21 segments makes

$$\Delta = \frac{0.47\lambda}{21} = 0.0224\lambda$$

Using (8-32) to compute E_z^i, the corresponding induced voltages obtained by multiplying the value of $-E_z^i$ at each segment by the length of the segment are listed in Table 8.1. where they are compared with those of the delta gap. In Table 8.1 $n = 1$ represents the outermost segment and $n = 11$ represents the center segment. Because of the symmetry, only values for the center segment and half of the other segments are shown. Although the two distributions are not identical, the magnetic-frill distribution voltages decay quite rapidly away from the center segment and they very quickly reach almost vanishing values.

Table 8.1 UNNORMALIZED AND NORMALIZED DIPOLE INDUCED VOLTAGE† DIFFERENCES FOR DELTA-GAP AND MAGNETIC-FRILL GENERATOR ($l = 0.47\lambda$, $a = 0.005\lambda$, $N = 21$)

Segment Number n	Delta-Gap Voltage		Magnetic Frill Generator Voltage			
	Unnormalized	Normalized	Unnormalized		Normalized	
1	0	0	1.11×10^{-4}	$-26.03°$	7.30×10^{-5}	$-26.03°$
2	0	0	1.42×10^{-4}	$-20.87°$	9.34×10^{-5}	$-20.87°$
3	0	0	1.89×10^{-4}	$-16.13°$	1.24×10^{-4}	$-16.13°$
4	0	0	2.62×10^{-4}	$-11.90°$	1.72×10^{-4}	$-11.90°$
5	0	0	3.88×10^{-4}	$-8.23°$	2.55×10^{-4}	$-8.23°$
6	0	0	6.23×10^{-4}	$-5.22°$	4.10×10^{-4}	$-5.22°$
7	0	0	1.14×10^{-3}	$-2.91°$	7.5×10^{-4}	$-2.91°$
8	0	0	2.52×10^{-3}	$-1.33°$	1.66×10^{-3}	$-1.33°$
9	0	0	7.89×10^{-3}	$-0.43°$	5.19×10^{-3}	$-0.43°$
10	0	0	5.25×10^{-2}	$-0.06°$	3.46×10^{-2}	$-0.06°$
11	1	1	1.52	0°	1.0	0°

†Voltage differences as defined here represent the product of the incident electric field at the center of each segment and the corresponding segment length.

8.4 MOMENT METHOD SOLUTION

Equations (8-22), (8-24), and (8-27) each has the form of

$$F(g) = h \tag{8-33}$$

where F is a known linear operator, h is a known excitation function, and g is the response function. For (8-22) F is an integrodifferential operator while for (8-24) and (8-27) it is an integral operator. The objective here is to determine g once F and h are specified.

While the inverse problem is often intractable in closed form, the linearity of the operator F makes a numerical solution possible. One technique, known as the Moment Method [7]–[14] requires that the unknown response function be expanded as a linear combination of N terms and written as

$$g(z') \simeq a_1 g_1(z') + a_2 g_2(z') + \cdots + a_N g_N(z') = \sum_{n=1}^{N} a_n g_n(z') \tag{8-34}$$

Each a_n is an unknown constant and each $g_n(z')$ is a known function usually referred to as a *basis* or *expansion* function. The domain of the $g_n(z')$ functions is the same as that of $g(z')$. Substituting (8-34) into (8-33) and using the linearity of the F operator reduces (8-33) to

$$\sum_{n=1}^{N} a_n F(g_n) = h \tag{8-35}$$

The basis functions g_n are chosen so that each $F(g_n)$ in (8-35) can be evaluated conveniently, preferably in closed form or at the very least numerically. The only task remaining then is to find the a_n unknown constants.

Expansion of (8-35) leads to one equation with N unknowns. It alone is not sufficient to determine the N unknown a_n ($n = 1, 2, \ldots, N$) constants. To resolve the N constants, it is necessary to have N linearly independent equations. This can be accomplished by evaluating (8-35) (e.g., applying boundary conditions) at N different points. This is referred to as *point-matching* (or *collocation*). Doing this, (8-35) takes the form of

$$\sum_{n=1}^{N} I_n F(g_n) = h_m, \qquad m = 1, 2, \ldots, N \tag{8-36}$$

In matrix form, (8-36) can be expressed as

$$[Z_{mn}][I_n] = [V_m] \tag{8-37}$$

where

$$Z_{mn} = F(g_n) \tag{8-37a}$$

$$I_n = a_n \tag{8-37b}$$

$$V_m = h_m \tag{8-37c}$$

The unknown coefficients a_n can be found by solving (8-37) using matrix inversion techniques, or

$$[I_n] = [Z_{mn}]^{-1}[V_m] \tag{8-38}$$

8.4.1 Basis Functions

One very important step in any numerical solution is the choice of basis functions. In general, one chooses as basis functions the set that has the ability to accurately represent and resemble the anticipated unknown function, while minimizing the computational effort required to employ it [28]–[30]. Do not choose basis functions with smoother properties than the unknown being represented.

Theoretically, there are many possible basis sets. However, only a limited number

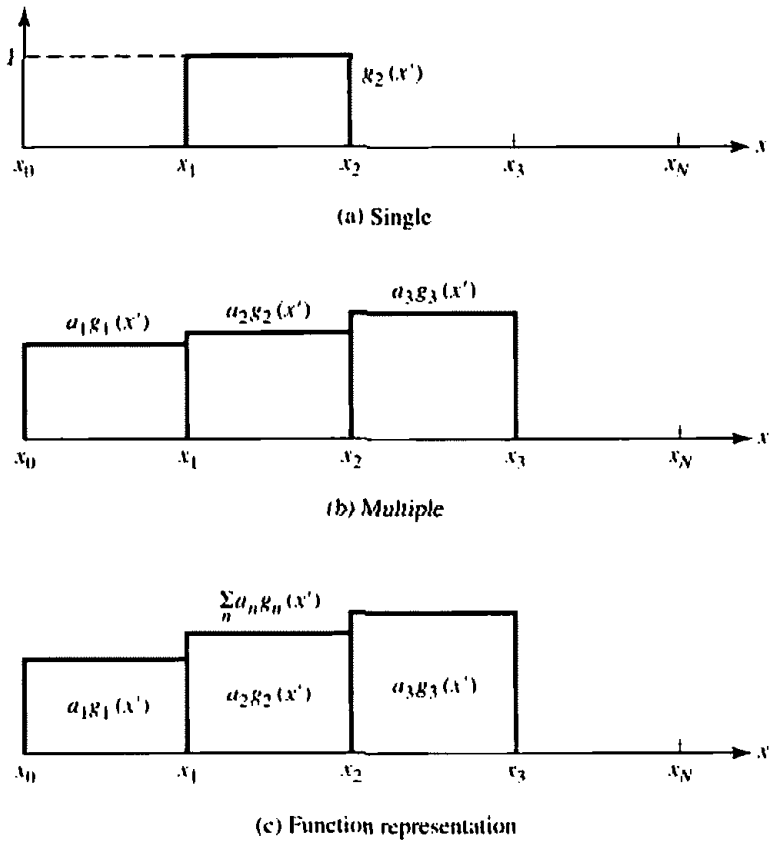

(a) Single

(b) Multiple

(c) Function representation

Figure 8.8 Piecewise constant subdomain functions.

are used in practice. These sets may be divided into two general classes. The first class consists of subdomain functions, which are nonzero only over a part of the domain of the function $g(x')$; its domain is the surface of the structure. The second class contains entire domain functions that exist over the entire domain of the unknown function. The entire domain basis function expansion is analogous to the well-known Fourier series expansion method.

A. Subdomain Functions

Of the two types of basis functions, subdomain functions are the most common. Unlike entire domain bases, they may be used without prior knowledge of the nature of the function that they must represent.

The subdomain approach involves subdivision of the structure into N nonoverlapping segments, as illustrated on the axis in Figure 8.8(a). For clarity, the segments are shown here to be collinear and of equal length, although neither condition is necessary. The basis functions are defined in conjunction with the limits of one or more of the segments.

Perhaps the most common of these basis functions is the conceptually simple piecewise constant, or "pulse" function, shown in Figure 8.8(a). It is defined by

Piecewise Constant

$$g_n(x') = \begin{cases} 1 & x'_{n-1} \le x' \le x'_n \\ 0 & \text{elsewhere} \end{cases} \tag{8-39}$$

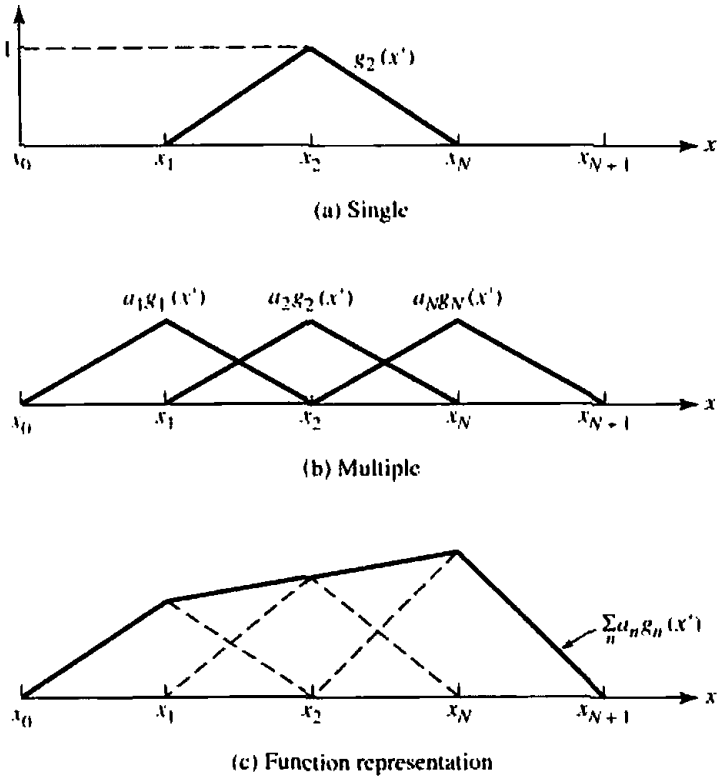

Figure 8.9 Piecewise linear subdomain functions.

Once the associated coefficients are determined, this function will produce a staircase representation of the unknown function, similar to that in Figures 8.8(b) and (c).

Another common basis set is the piecewise linear, or "triangle," functions seen in Figure 8.9(a). These are defined by

Piecewise Linear

$$g_n(x') = \begin{cases} \dfrac{x' - x'_{n-1}}{x'_n - x'_{n-1}} & x'_{n-1} \le x' \le x'_n \\ \dfrac{x'_{n+1} - x'}{x'_{n+1} - x'_n} & x'_n \le x' \le x'_{n+1} \\ 0 & \text{elsewhere} \end{cases} \tag{8-40}$$

and are seen to cover two segments, and overlap adjacent functions [Figure 8.9(b)]. The resulting representation [Figure 8.9(c)] is smoother than that for "pulses," but at the cost of increased computational complexity.

Increasing the sophistication of subdomain basis functions beyond the level of the "triangle" may not be warranted by the possible improvement in accuracy. However, there are cases where more specialized functions are useful for other reasons. For example, some integral operators may be evaluated without numerical integration when their integrands are multiplied by a $\sin(kx')$ or $\cos(kx')$ function, where x' is the variable of integration. In such examples, considerable advantages in computation time and resistance to errors can be gained by using basis functions like the piecewise sinusoid of Figure 8.10 or truncated cosine of Figure 8.11. These functions are defined by

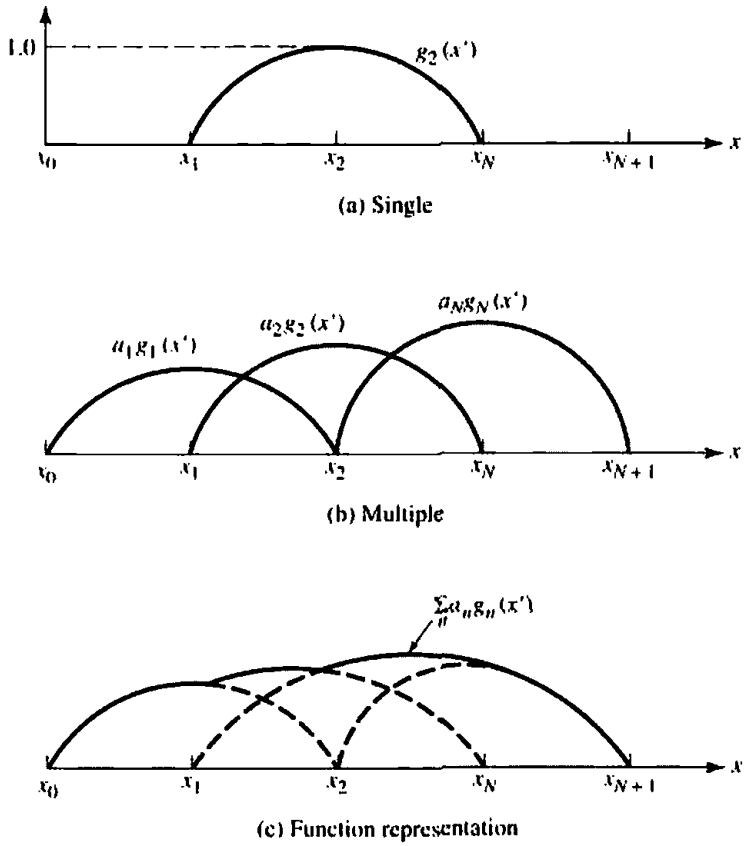

Figure 8.10 Piecewise sinusoids subdomain functions.

Piecewise Sinusoid

$$g_n(x') = \begin{cases} \dfrac{\sin[k(x' - x'_{n-1})]}{\sin[k(x'_n - x'_{n-1})]} & x'_{n-1} \le x' \le x'_n \\ \dfrac{\sin[k(x'_{n+1} - x')]}{\sin[k(x'_{n+1} - x'_n)]} & x'_n \le x' \le x'_{n+1} \\ 0 & \text{elsewhere} \end{cases} \tag{8-41}$$

Truncated Cosine

$$g_n(x') = \begin{cases} \cos\left[k\left(x' - \dfrac{x'_n - x'_{n-1}}{2}\right)\right] & x'_{n-1} \le x' \le x'_n \\ 0 & \text{elsewhere} \end{cases} \tag{8-42}$$

B. Entire Domain Functions

Entire domain basis functions, as their name implies, are defined and are nonzero over the entire length of the structure being considered. Thus no segmentation is involved in their use.

A common entire domain basis set is that of sinusoidal functions, where

Entire Domain

$$g_n(x') = \cos\left[\frac{(2n-1)\pi x'}{l}\right] \qquad -\frac{l}{2} \le x' \le \frac{l}{2} \tag{8-43}$$

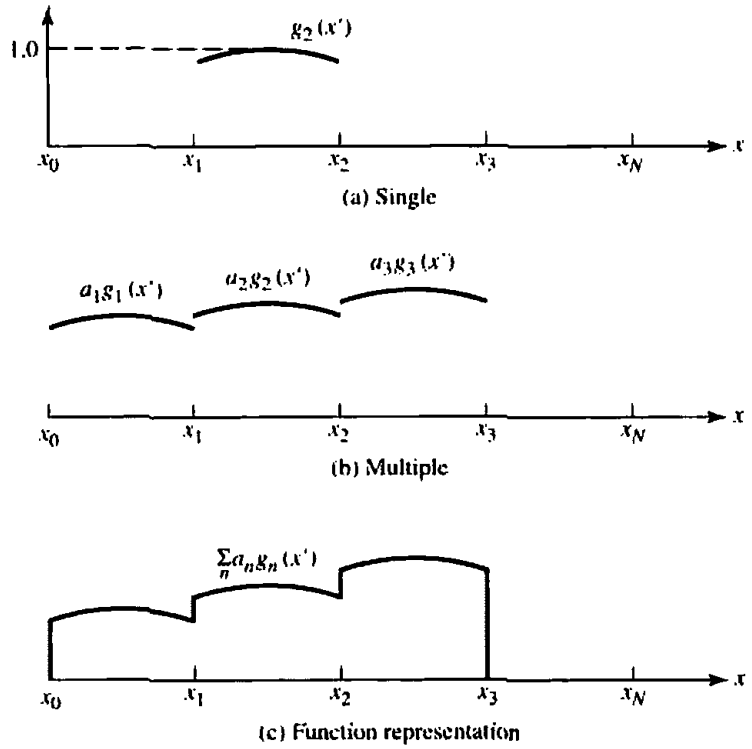

Figure 8.11 Truncated cosines subdomain functions.

Note that this basis set would be particularly useful for modeling the current distribution on a wire dipole, which is known to have primarily sinusoidal distribution. The main advantage of entire domain basis functions lies in problems where the unknown function is assumed *a priori* to follow a known pattern. Such entire-domain functions may render an acceptable representation of the unknown while using far fewer terms in the expansion of (8-34) than would be necessary for subdomain bases. Representation of a function by entire domain cosine and/or sine functions is similar to the Fourier series expansion of arbitrary functions.

Because we are constrained to use a finite number of functions (or modes, as they are sometimes called), entire domain basis functions usually have difficulty in modeling arbitrary or complicated unknown functions.

Entire domain basis functions, sets like (8-43), can be generated using Tschebyscheff, Maclaurin, Legendre, and Hermite polynomials, or other convenient functions.

8.4.2 Weighting (Testing) Functions

To improve the point-matching solution of (8-36), (8-37), or (8-38) an inner product $\langle w, g \rangle$ can be defined which is a scalar operation satisfying the laws of

$$\langle w, g \rangle = \langle g, w \rangle \tag{8-44a}$$

$$\langle bf + cg, w \rangle = b\langle f, w \rangle + c\langle g, w \rangle \tag{8-44b}$$

$$\langle g^*, g \rangle > 0 \quad \text{if } g \neq 0 \tag{8-44c}$$

$$\langle g^*, g \rangle = 0 \quad \text{if } g = 0 \tag{8-44d}$$

where b and c are scalars and the asterisk (*) indicates complex conjugation. A typical, but not unique, inner product is

$$\langle \mathbf{w}, \mathbf{g} \rangle = \iint_s \mathbf{w}^* \cdot \mathbf{g}\, ds \tag{8-45}$$

where the w's are the *weighting* (*testing*) functions and S is the surface of the structure being analyzed. Note that the functions w and g can be vectors. This technique is better known as the *Moment Method* or *Method of Moments* (MM) [7], [8].

The collocation (point-matching) method is a numerical technique whose solutions satisfy the electromagnetic boundary conditions (e.g., vanishing tangential electric fields on the surface of an electric conductor) only at discrete points. Between these points the boundary conditions may not be satisfied, and we define the deviation as a *residual* (e.g., residual $= \Delta E|_{\tan} = E\text{ (scattered)}|_{\tan} + E\text{ (incident)}|_{\tan} \neq 0$ on the surface of an electric conductor). For a half-wavelength dipole, a typical residual is shown in Figure 8.12(a) for pulse basis functions and point-matching and Figure 8.12(b) exhibits the residual for piecewise sinusoids-Galerkin method [31]. As expected, the pulse basis point-matching exhibits the most ill-behaved residual and the piecewise sinusoids-Galerkin method indicates an improved residual. To minimize the residual in such a way that its overall average over the entire structure approaches zero, the method of *weighted residuals* is utilized in conjunction with the inner product of (8-45). This technique, referred to as the *Moment Method* (MM), does not lead to a vanishing residual at every point on the surface of a conductor, but it forces the boundary conditions to be satisfied in an average sense over the entire surface.

To accomplish this, we define a set of N *weighting* (or testing) functions $\{w_m\} = w_1, w_2, \ldots, w_N$ in the domain of the operator F. Forming the inner product between each of these functions, (8-35) results in

$$\sum_{n=1}^{N} a_n \langle w_m, F(g_n) \rangle = \langle w_m, h \rangle \qquad m = 1, 2, \ldots, N \tag{8-46}$$

This set of N equations may be written in matrix form as

$$[F_{mn}]\,[a_n] = [h_m] \tag{8-47}$$

where

$$[F_{mn}] = \begin{bmatrix} \langle w_1, F(g_1) \rangle & \langle w_1, F(g_2) \rangle & \cdots \\ \langle w_2, F(g_1) \rangle & \langle w_2, F(g_2) \rangle & \\ \vdots & & \vdots \end{bmatrix} \tag{8-47a}$$

$$[a_n] = \begin{bmatrix} a_1 \\ a_2 \\ \vdots \\ a_N \end{bmatrix} \qquad [h_m] = \begin{bmatrix} \langle w_1, h \rangle \\ \langle w_2, h \rangle \\ \vdots \\ \langle w_N, h \rangle \end{bmatrix} \tag{8-47b}$$

The matrix of (8-47) may be solved for the a_n by inversion, and it can be written as

$$[a_n] = [F_{mn}]^{-1}[h_m] \tag{8-48}$$

The choice of weighting functions is important in that the elements of $\{w_n\}$ must be linearly independent, so that the N equations in (8-46) will be linearly independent [7]–[9], [29], [30]. Further, it will generally be advantageous to choose weighting functions that minimize the computations required to evaluate the inner product.

The condition of linear independence between elements and the advantage of

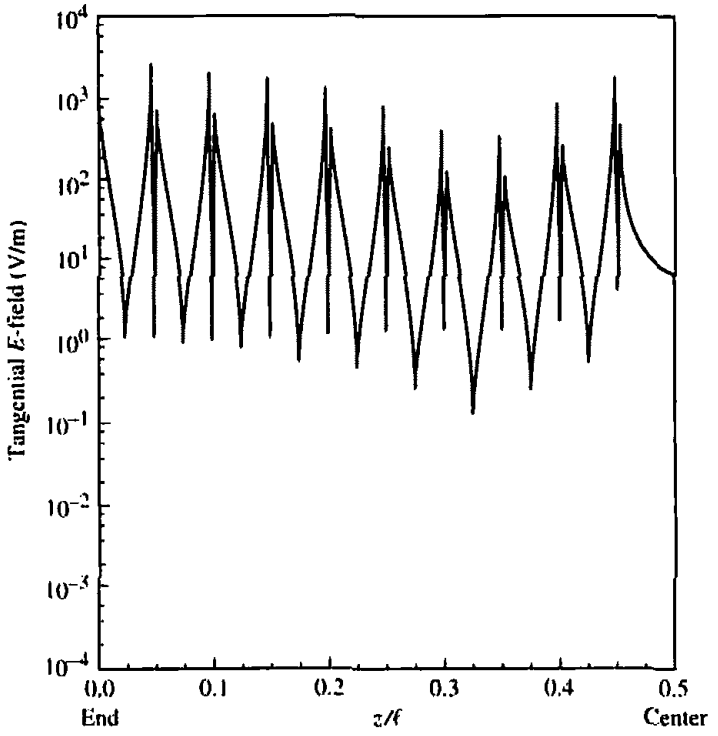

(a) Pulse point-matching

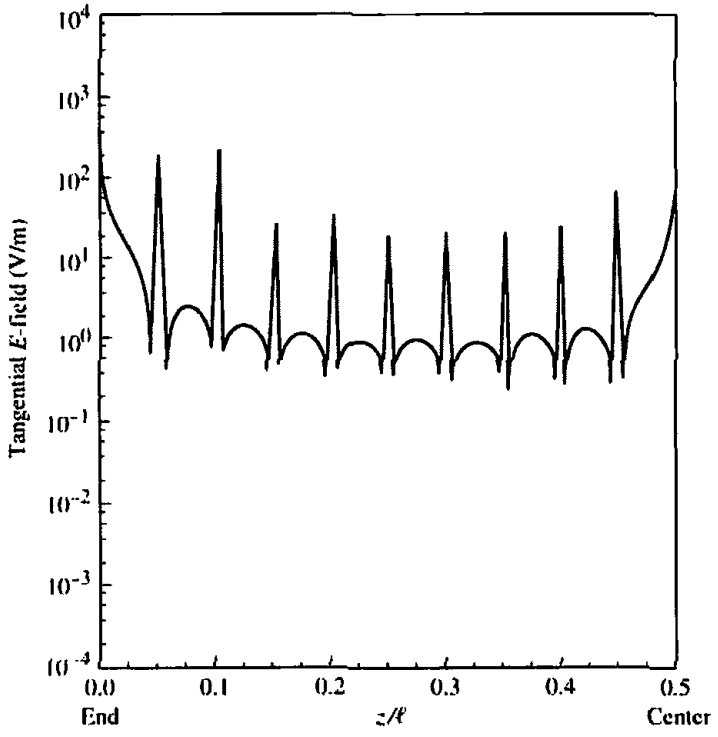

(b) Piecewise sinusoids-Galerkin

Figure 8.12 Tangential electric field on the conducting surface of a $\lambda/2$ dipole. (SOURCE: E. K. Miller and F. J. Deadrick, "Some computational aspects of thin-wire modeling" in *Numerical and Asymptotic Techniques in Electromagnetics*, 1975, Springer-Verlag.)

computational simplicity are also important characteristics of basis functions. Because of this, similar types of functions are often used for both weighting and expansion. A particular choice of functions may be to let the weighting and basis function be the same, that is, $w_n = g_n$. This technique is known as *Galerkin's method* [32].

It should be noted that there are N^2 terms to be evaluated in (8-47a). Each term usually requires two or more integrations; at least one to evaluate each $F(g_n)$ and one to perform the inner products of (8-45). When these integrations are to be done numerically, as is often the case, vast amounts of computation time may be necessary. There is, however, a unique set of weighting functions that reduce the number of required integrations. This is the set of Dirac delta weighting functions

$$[w_m] = [\delta(p - p_m)] = [\delta(p - p_1), \delta(p - p_2), \ldots] \tag{8-49}$$

where p specifies a position with respect to some reference (origin) and p_m represents a point at which the boundary condition is enforced. Using (8-45) and (8-49) reduces (8-46) to

$$\begin{aligned} \langle \delta(p - p_m), h \rangle &= \sum_n a_n \langle \delta(p - p_m), F(g_n) \rangle \quad m = 1, 2, \ldots, N \\ \iint_S \delta(p - p_m) h \, ds &= \sum_n a_n \iint_S \delta(p - p_m) F(g_n) \, ds \quad m = 1, 2, \ldots, N \\ h|_{p=p_m} &= \sum_n a_n F(g_n)|_{p=p_m} \quad m = 1, 2, \ldots, N \end{aligned} \tag{8-50}$$

Hence, the only remaining integrations are those specified by $F(g_n)$. This simplification may lead to solutions that would be impractical if other weighting functions were used. Physically, the use of Dirac delta weighting functions is seen as the relaxation of boundary conditions so that they are enforced only at discrete points on the surface of the structure, hence the name point-matching.

An important consideration when using point-matching is the positioning of the N points (p_m). While equally space points often yield good results, much depends on the basis functions used. When using subsectional basis functions in conjunction with point-matching, one match point should be placed on each segment (to maintain linear independence). Placing the points at the center of the segments usually produces the best results. It is important that a match point does not coincide with the "peak" of a triangle or a similar discontinuous function, where the basis function is not differentiably continuous. This may cause errors in some situations.

8.5 SELF IMPEDANCE

The input impedance of an antenna is a very important parameter, and it is used to determine the efficiency of the antenna. In Section 4.5 the real part of the impedance (referred either to the current at the feed terminals or to the current maximum) was found. At that time, because of mathematical complexities, no attempt was made to find the imaginary part (reactance) of the impedance. In this section the self impedance of a linear element will be examined using both the Integral Equation-Moment Method and the induced emf method. The real and imaginary parts of the impedance will be found using both methods.

8.5.1 Integral Equation-Moment Method

To use this method to find the self impedance of a dipole, the first thing to do is to solve the integral equation for the current distribution. This is accomplished using either Pocklington's Integral equation of (8-22) or (8-24) or Hallén's integral equation of (8-27). For Pocklington's integral equation you can use either the delta-gap voltage excitation of (8-28) or the magnetic frill model of (8-31) or (8-32). Hallén's integral equation is based on the delta-gap model of (8-28).

Once the current distribution is found, using either or both of the integral equations, then the self (input) impedance is determined using the ratio of the voltage to current, or

$$Z_{in} = \frac{V_{in}}{I_{in}} \tag{8-51}$$

A computer program MOMENT METHOD has been developed based on Pocklington's and Hallén's integral equations, and it is found at the end of this chapter. Pocklington's uses both the delta-gap and magnetic-frill models while Hallén's uses only the delta-gap feed model. Both, however, use piecewise constant subdomain functions and point-matching. The program computes the current distribution, normalized amplitude radiation pattern, and input impedance. The user must specify the *length of the wire, its radius (both in wavelengths), and the type of feed modeling* (delta-gap or magnetic-frill) and the number of segments.

To demonstrate the procedure and compare the results using the two-source modelings (delta-gap and magnetic-frill generator) for Pocklington's integral equation, an example is performed.

Example 8.4

Assume a center-fed linear dipole of $l = 0.47\lambda$ and $a = 0.005\lambda$. This is the same element of Example 8.3.

1. Determine the normalized current distribution over the length of the dipole using $N = 21$ segments to subdivide the length. Plot the current distribution.
2. Determine the input impedance using segments of $N = 7, 11, 21, 29, 41, 51, 61, 71$, and 79.

Use Pocklington's integrodifferential equation (8-24) with piecewise constant subdomain basis functions and point-matching to solve the problems, model the gap with one segment, and use both the delta-gap and magnetic-frill generator to model the excitation. Use (8-32) for the magnetic-frill generator. Because the current at the ends of the wire vanishes, the piecewise constant subdomain basis functions are not the most judicious choice. However, because of their simplicity, they are chosen here to illustrate the principles even though the results are not the most accurate. Assume that the characteristic impedance of the annular aperture is 50 ohms and the excitation voltage V_i is 1 V.

SOLUTION

1. The voltage distribution was found in Example 8.3, and it is listed in Table 8.1. The corresponding normalized currents obtained using (8-24) with piecewise constant pulse functions and point-matching technique for both the delta-gap and magnetic frill-generator are shown plotted in Figure 8.13(a). It is apparent that the two distributions are almost identical in shape, and they resemble that of the ideal sinusoidal current distribution which is more valid for very thin wires and very small gaps. The distributions obtained using Pocklington's integral equation do not vanish at the ends because of the use of piecewise constant subdomain basis functions.

Table 8.2 DIPOLE INPUT IMPEDANCE FOR DELTA-GAP AND MAGNETIC-FRILL GENERATOR USING POCKLINGTON'S INTEGRAL EQUATION ($l = 0.47\lambda$, $a = 0.005\lambda$)

N	Delta Gap	Magnetic Frill
7	122.8 + j113.9	26.8 + j24.9
11	94.2 + j49.0	32.0 + j16.7
21	77.7 − j0.8	47.1 − j0.2
29	75.4 − j6.6	57.4 − j4.5
41	75.9 − j2.4	68.0 − j1.0
51	77.2 + j2.4	73.1 + j4.0
61	78.6 + j6.1	76.2 + j8.5
71	79.9 + j7.9	77.9 + j11.2
79	80.4 + j8.8	78.8 + j12.9

2. The input impedances using both the delta-gap and the magnetic-frill generator are shown listed in Table 8.2. It is evident that the values begin to stabilize and compare favorably to each other once 61 or more segments are used.

To further illustrate the point on the variation of the current distribution on a dipole, it has been computed by Moment Method and plotted in Figure 8.13(b) for $l = \lambda/2$ and $l = \lambda$ for wire radii of a = $10^{-5}\lambda$ and $10^{-3}\lambda$ where it is compared with that based on the sinusoidal distribution. It is apparent that the radius of the wire does not influence to a large extent the distribution of the $l = \lambda/2$ dipole. However it has a profound effect on the current distribution of the $l = \lambda$ dipole at and near the feed point. Therefore the input impedance of the $l = \lambda$ dipole is quite different for the three cases of Figure 8.13(b), since the zero current at the center of the sinusoidal distribution predicts an infinite impedance. In practice, the impedance is not infinite but is very large.

8.5.2 Induced EMF Method

The induced emf method is a classical method to compute the self and mutual impedances [1]–[6], [33]. The method is basically limited to straight, parallel and in echelon elements, and it is more difficult to account accurately for the radius of the wires as well as the gaps at the feeds. However it leads to closed form solutions which provide very good design data. From the analysis of the infinitesimal dipole in Section 4.2, it was shown that the imaginary part of the power density, which contributes to the imaginary power, is dominant in the near-zone of the element and becomes negligible in the far-field. Thus, near-fields of an antenna are required to find its input reactance.

A. Near-Field of Dipole

In Chapter 4 the far-zone electric and magnetic fields radiated by a finite length dipole with a sinusoidal current distribution were found. The observations were restricted in the far-field in order to reduce the mathematical complexities. The expressions of these fields were used to derive the radiation resistance and the input resistance of the

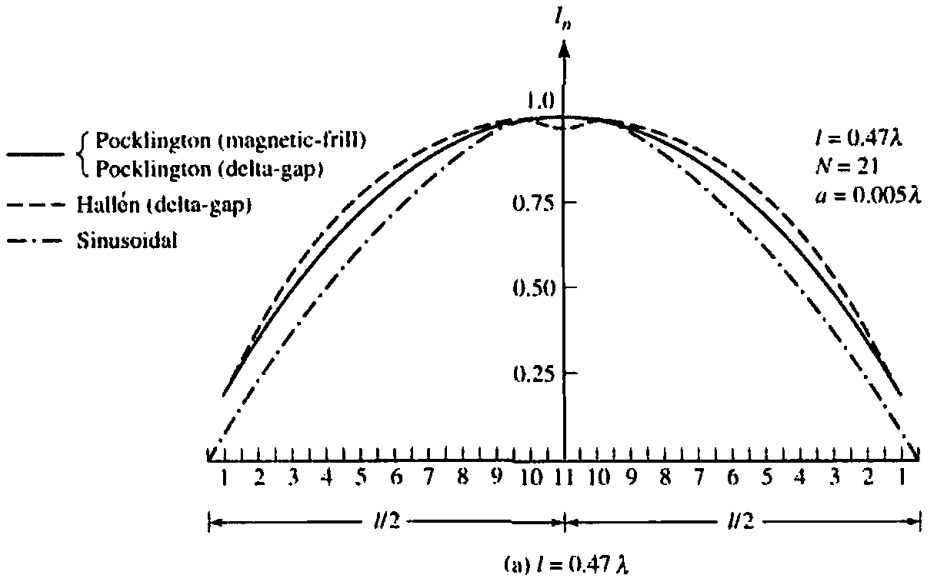

(a) $l = 0.47\,\lambda$

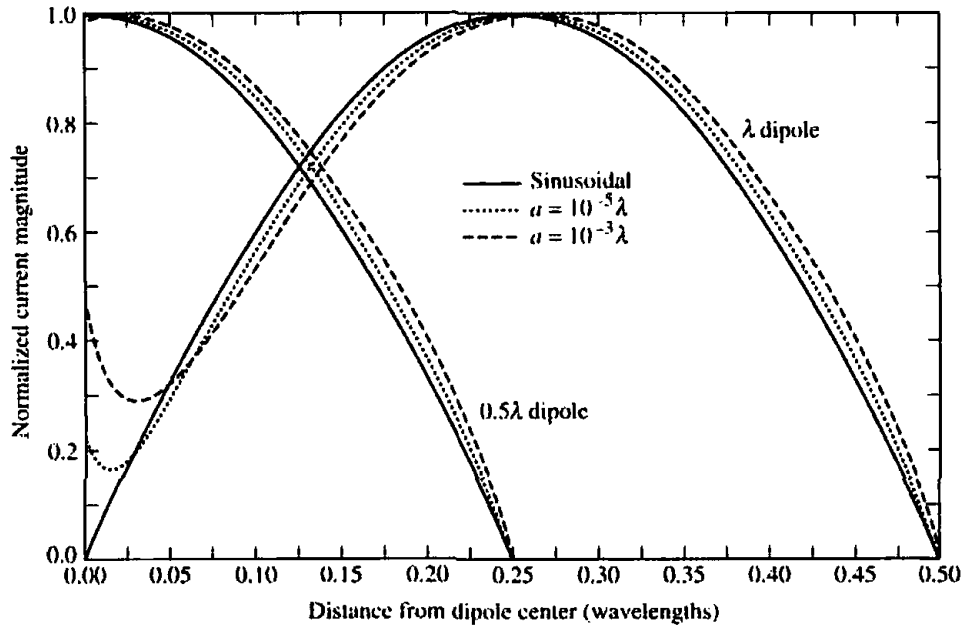

(b) $l \approx \lambda/2$ and $l = \lambda$

Figure 8.13 Current distribution on a dipole antenna.

dipole. However, when the input reactance and/or the mutual impedance between elements are desired, the near-fields of the element must be known. It is the intent here to highlight the derivation.

The fields are derived based on the geometry of Figure 8.14. The procedure is identical to that used in Section 4.2.1 for the infinitesimal dipole. The major difference is that the integrations are much more difficult. To minimize long derivations involving complex integrations, only the procedure will be outlined and the final results will be given. The derivation is left as an end of the chapter problems. The details can also be found in the first edition of this book.

To derive the fields, the first thing is to specify the sinusoidal current distribution for a finite dipole which is that of (4-56). Once that is done, then the vector potential **A** of (4-2) is determined. Then the magnetic field is determined using (3-2a), or

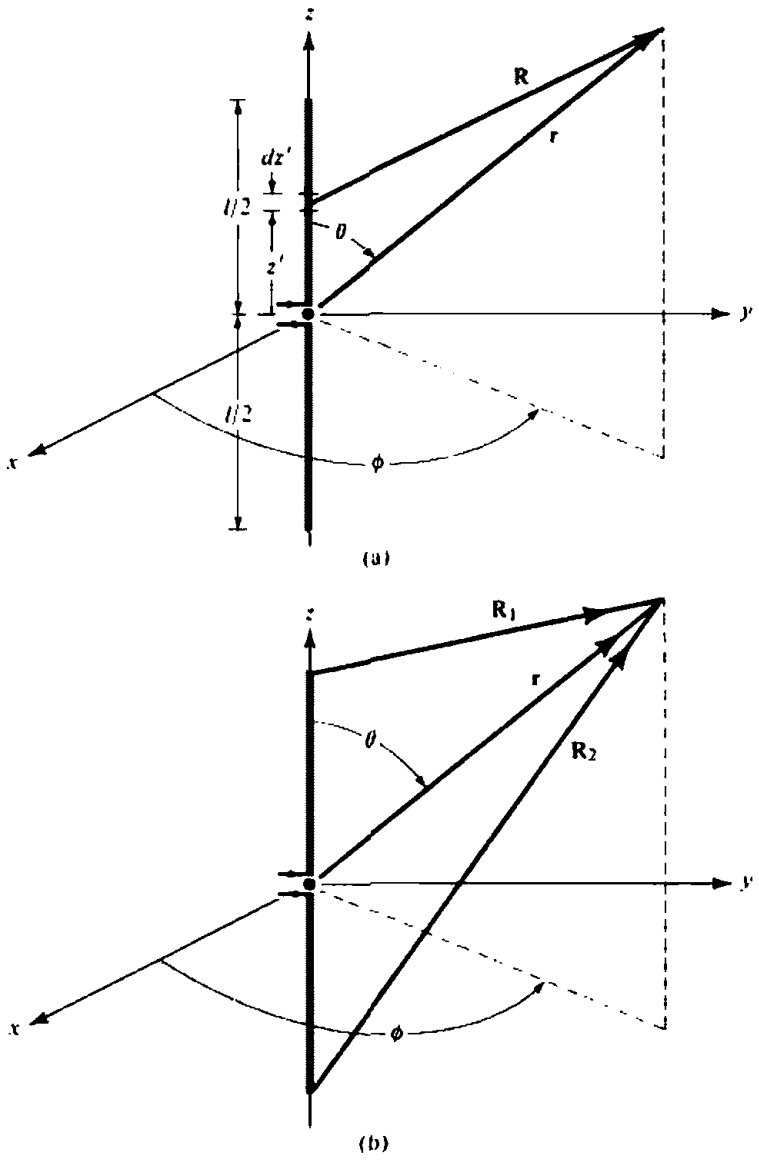

Figure 8.14 Dipole geometry for near-field analysis.

$$\mathbf{H} = \frac{1}{\mu}\nabla \times \mathbf{A} = -\hat{\mathbf{a}}_\phi \frac{1}{\mu}\frac{\partial A_z}{\partial \rho} \tag{8-52}$$

It is recommended that cylindrical coordinates are used. By following this procedure and after some lengthy analytical details, it can be shown by referring to Figure 8.14(b) that the magnetic field radiated by the dipole is

$$\mathbf{H} = \hat{\mathbf{a}}_\phi H_\phi = -\hat{\mathbf{a}}_\phi \frac{I_0}{4\pi j}\frac{1}{y}\left[e^{-jkR_1} + e^{-jkR_2} - 2\cos\left(\frac{kl}{2}\right)e^{-jkr}\right] \tag{8-53}$$

where

$$r = \sqrt{x^2 + y^2 + z^2} = \sqrt{\rho^2 + z^2} \tag{8-53a}$$

$$R_1 = \sqrt{x^2 + y^2 + \left(z - \frac{l}{2}\right)^2} = \sqrt{\rho^2 + \left(z - \frac{l}{2}\right)^2} \tag{8-53b}$$

$$R_2 = \sqrt{x^2 + y^2 + \left(z + \frac{l}{2}\right)^2} = \sqrt{\rho^2 + \left(z + \frac{l}{2}\right)^2} \tag{8-53c}$$

The corresponding electric field is found using Maxwell's equation of

$$\mathbf{E} = \frac{1}{j\omega\epsilon}\nabla \times \mathbf{H} \tag{8-54}$$

Once this is done, it can be shown that the electric field radiated by the dipole is

$$\mathbf{E} = \hat{\mathbf{a}}_\rho E_\rho + \hat{\mathbf{a}}_z E_z = -\hat{\mathbf{a}}_\rho \frac{1}{j\omega\epsilon}\frac{\partial H_\phi}{\partial z} + \hat{\mathbf{a}}_z \frac{1}{j\omega\epsilon}\frac{1}{\rho}\frac{\partial}{\partial \rho}(\rho H_\phi) \tag{8-55}$$

where

$$E_\rho = E_r = j\frac{\eta I_0}{4\pi}\left[\left(z - \frac{l}{2}\right)\frac{e^{-jkR_1}}{R_1} + \left(z + \frac{l}{2}\right)\frac{e^{-jkR_2}}{R_2} - 2z\cos\left(\frac{kl}{2}\right)\frac{e^{-jkr}}{r}\right] \tag{8-55a}$$

$$E_z = -j\frac{\eta I_0}{4\pi}\left[\frac{e^{-jkR_1}}{R_1} + \frac{e^{-jkR_2}}{R_2} - 2\cos\left(\frac{kl}{2}\right)\frac{e^{-jkr}}{r}\right] \tag{8-55b}$$

It should be noted that the last term in (8-53), (8-55a), and (8-55b) vanishes when the overall length of the element is an integral number of odd half wavelengths ($l = n\lambda/2$, $n = 1, 3, 5, \ldots$) because $\cos(kl/2) = \cos(n\pi/2) = 0$ for $n = 1, 3, 5, \ldots$.

The fields of (8-53), (8-55a), and (8-55b) were derived assuming a zero radius wire. In practice all wire antennas have a finite radius which in most cases is very small electrically (typically less than $\lambda/200$). Therefore the fields of (8-53), (8-55a), and (8-55b) are good approximations for finite, but small, radius dipoles.

B. Self Impedance

The technique, which is used in this chapter to derived closed form expressions for the self- and driving point impedances of finite linear dipoles, is known as the *induced emf method*. The general approach of this method is to form the Poynting vector using (8-53), (8-55a), and (8-55b), and to integrate it over the surface that coincides with the surface of the antenna (linear dipole) itself. However, the same results can be obtained using a slightly different approach, as will be demonstrated here. The expressions derived using this method are more valid for small radii dipoles. Expressions, which are more accurate for larger radii dipoles, were derived in the previous section based on the Integral Equation-Moment Method.

To find the input impedance of a linear dipole of finite length and radius, shown in Figure 8.15, the tangential electric field component on the surface of the wire is needed. This was derived previously and is represented by (8-55b). Based on the current distribution and tangential electric field along the surface of the wire, the induced potential developed at the terminals of the dipole based on the maximum current is given by

$$V_m = \int_{-\ell/2}^{+\ell/2} dV_m$$

$$= -\frac{1}{I_m}\int_{-\ell/2}^{+\ell/2} I_z(\rho = a, z = z')E_z(\rho = a, z = z')\,dz' \tag{8-56}$$

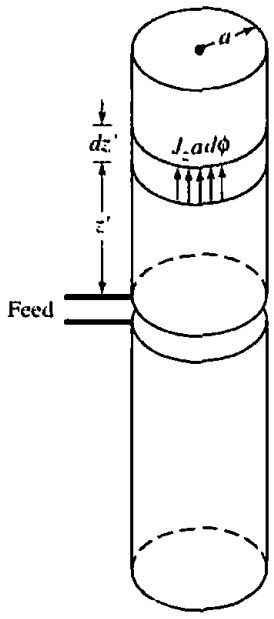

Figure 8.15 Uniform linear current density over cylindrical surface of wire.

where I_m is the maximum current. The input impedance (*referred to at the current maximum* I_m) is defined as

$$Z_{in} = \frac{V_m}{I_m} \tag{8-57}$$

and can be expressed using (8-56) as

$$Z_{in} = -\frac{1}{I_m^2}\int_{-\ell/2}^{\ell/2} I_z(\rho = a, z = z')E_z(\rho = a, z = z')\,dz' \tag{8-57a}$$

Equation (8-57a) can also be obtained by forming the complex power density, integrating it over the surface of the antenna, and then relating the complex power to the terminal and induced voltages [2]. The integration can be performed either over the gap at the terminals or over the surface of the conducting wire.

For a wire dipole, the total current I_z is uniformly distributed around the surface of the wire, and it forms a linear current sheet J_z. The current is concentrated primarily over a very small thickness of the conductor, as shown in Figure 8.15, and it is given, based on (4-56), by

$$I_z = 2\pi a J_z = I_m \sin\left[k\left(\frac{l}{2} - |z'|\right)\right] \tag{8-58}$$

Therefore (8-57a) can be written as

$$Z_{in} = -\frac{1}{I_m}\int_{-\ell/2}^{\ell/2} \sin\left[k\left(\frac{l}{2} - |z'|\right)\right] E_z(\rho = a, z = z')\,dz' \tag{8-59}$$

For simplicity, it is assumed that the E-field produced on the surface of the wire by a current sheet is the same as if the current were concentrated along a filament placed along the axis of the wire. Then the E-field used in (8-59) is the one obtained along a line parallel to the wire at a distance $\rho = a$ from the filament.

Letting $I_m = I_0$ and substituting (8-55b) into (8-59) it can be shown, after some

lengthy but straightforward manipulations, that the real and imaginary parts of the input impedance (referred to at the *current maximum*) can be expressed as

$$R_r = R_m = \frac{\eta}{2\pi}\{C + \ln(kl) - C_i(kl) + \frac{1}{2}\sin(kl)[S_i(2kl) - 2S_i(kl)] + \frac{1}{2}\cos(kl)[C + \ln(kl/2) + C_i(2kl) - 2C_i(kl)]\} \tag{8-60a}$$

$$X_m = \frac{\eta}{4\pi}\left\{2S_i(kl) + \cos(kl)[2S_i(kl) - S_i(2kl)] - \sin(kl)\left[2C_i(kl) - C_i(2kl) - C_i\left(\frac{2ka^2}{l}\right)\right]\right\} \tag{8-60b}$$

where $S_i(x)$ and $C_i(x)$ are the sine and cosine integrals of Appendix III. Equation (8-60a) is identical to (4-70). In deriving (8-60a) it was assumed that the radius of the wire is negligible (in this case set to zero), and it has little effect on the overall answer. This is a valid assumption provided $l \gg a$, and it has been confirmed by other methods.

The input resistance and input reactance (*referred to at the current at the input terminals*) can be obtained by a transfer relation given by (4-79), or

$$R_{in} = \left(\frac{I_0}{I_{in}}\right)^2 R_r = \frac{R_r}{\sin^2(kl/2)} \tag{8-61a}$$

$$X_{in} = \left(\frac{I_0}{I_{in}}\right)^2 X_m = \frac{X_m}{\sin^2(kl/2)} \tag{8-61b}$$

For a small dipole the input reactance is given by [34]

$$X_{in} = X_m = -120\frac{[\ln(l/2a) - 1]}{\tan(kl/2)} \tag{8-62}$$

while its input resistance and radiation resistance are given by (4-37). Plots of the self impedance, both resistance and reactance, based on (8-60a), (8-60b) and (8-61a), (8-61b) for $0 \le l \le 3\lambda$ are shown in Figures 8.16(a,b). The radius of the wire is $10^{-5}\lambda$. It is evident that when the length of the wire is multiples of a wavelength the resistances and reactances become infinite; in practice they are large.

Ideally the radius of the wire does not affect the input resistance, as is indicated by (8-60a). However in practice it does have an effect, although it is not as significant as it is for the input reactance. To examine the effect the radius has on the values of the reactance, its values as given by (8-60) have been plotted in Figure 8.17 for $a = 10^{-5}\lambda$, $10^{-4}\lambda$, $10^{-3}\lambda$, and $10^{-2}\lambda$. The overall length of the wire is taken to be $0 < l \le 3\lambda$. It is apparent that the reactance can be reduced to zero provided the overall length is slightly less than $n\lambda/2$, $n = 1, 3, \ldots$, or slightly greater than $n\lambda/2$, $n = 2, 4, \ldots$. This is commonly done in practice for $l \simeq \lambda/2$ because the input resistance is close to 50 ohms, an almost ideal match for the widely used 50-ohm lines. For small radii, the reactance for $l = \lambda/2$ is equal to 42.5 ohms.

From (8-60b) it is also evident that when $l = n\lambda/2$, $n = 1, 2, 3, \ldots$, the terms within the last bracket do not contribute because $\sin(kl) = \sin(n\pi) = 0$. Thus for dipoles whose overall length is an integral number of half-wavelengths, the radius

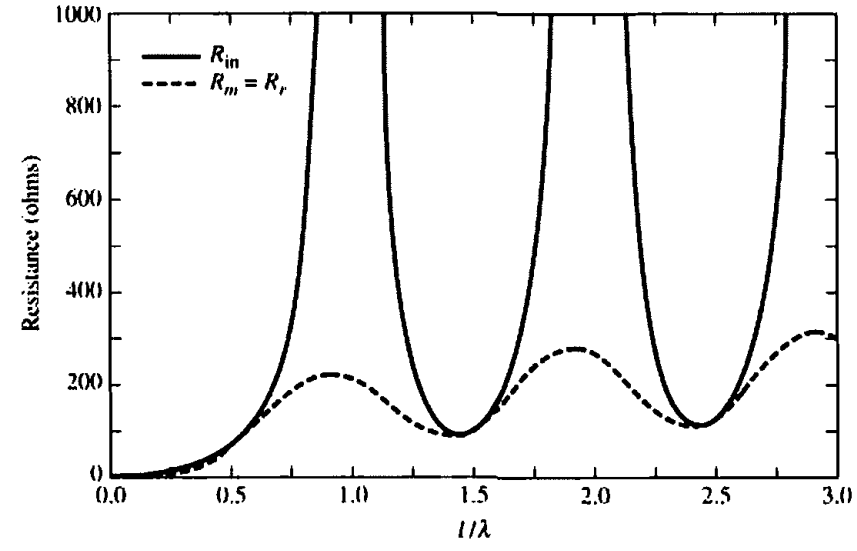

(a) Resistance

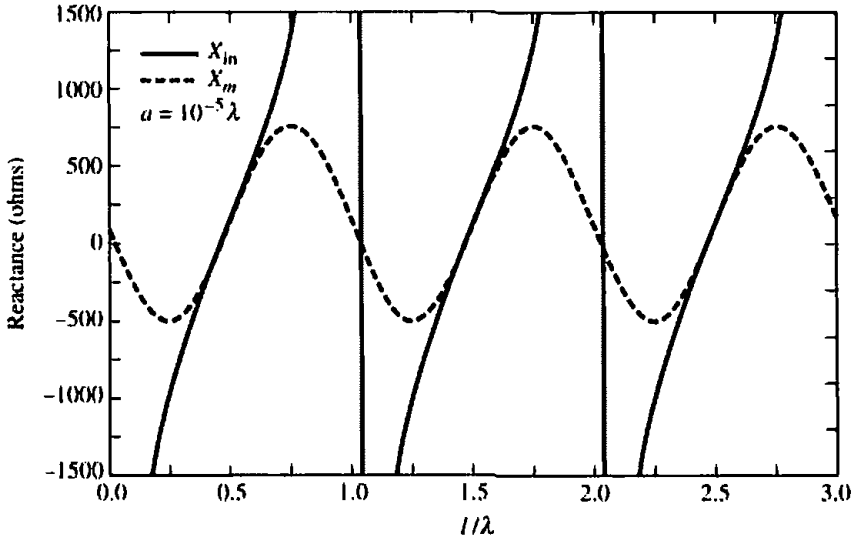

(b) Reactance

Figure 8.16 Self-resistance and self-reactance of dipole antenna with wire radius of $10^{-5}\ \lambda$.

has no effect on the antenna reactance. This is illustrated in Figure 8.17 by the intersection points of the curves.

Example 8.5

Using the induced emf method, compute the input reactance for a linear dipole whose lengths are $n\lambda/2$, where $n = 1 - 6$.

SOLUTION

The input reactance for a linear dipole based on the induced emf method is given by (8-60b) whose values are equal to 42.5 for $\lambda/2$, 125.4 for λ, 45.5 for $3\lambda/2$, 133.1 for 2λ, 46.2 for $5\lambda/2$, and 135.8 for 3λ.

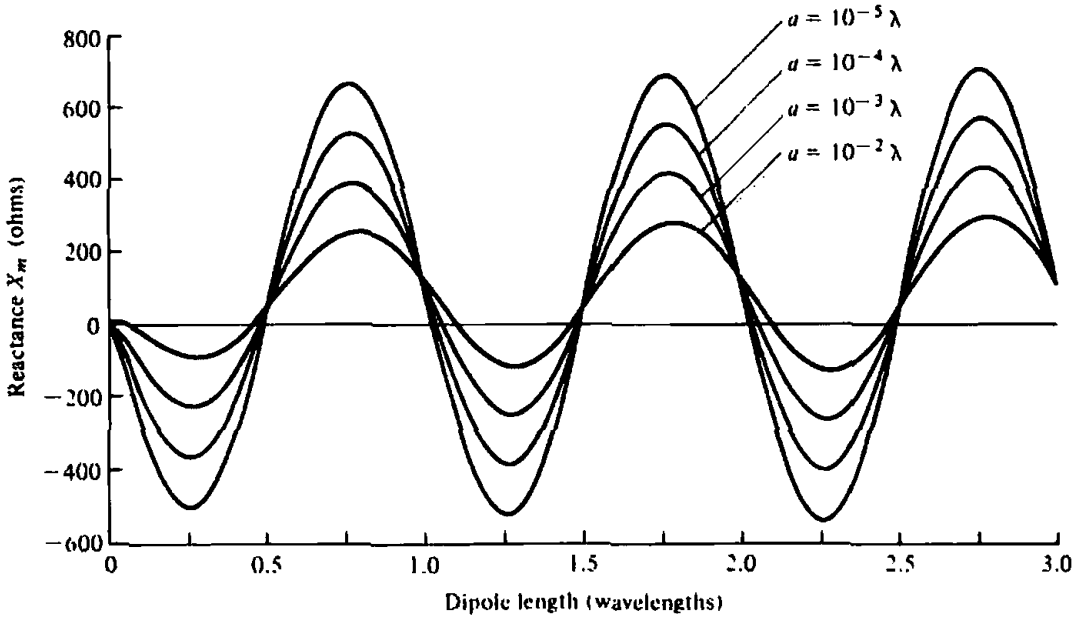

Figure 8.17 Reactance (referred to the current maximum) of linear dipole with sinusoidal current distribution for different wire radii.

8.6 MUTUAL IMPEDANCE BETWEEN LINEAR ELEMENTS

In the previous section, the input impedance of a linear dipole was derived when the element was radiating into an unbounded medium. The presence of an obstacle, which could be another element, would alter the current distribution, the field radiated, and in turn the input impedance of the antenna. Thus the antenna performance depends not only on its own current but also on the current of neighboring elements. For resonant elements with no current excitation of their own, there could be a substantial current induced by radiation from another source. These are known as parasitic elements, as in the case of a Yagi-Uda antenna, and play an important role in the overall performance of the entire antenna system. The antenna designer, therefore, must take into account the interaction and mutual effects between elements. The input impedance of the antenna in the presence of the other elements or obstacles, which will be referred to as *driving-point impedance*, depends upon the self impedance (input impedance in the absence of any obstacle or other element) and the mutual impedance between the driven element and the other obstacles or elements.

To simplify the analysis, it is assumed that the antenna system consists of two elements. The system can be represented by a two-port (four-terminal) network, as shown in Figure 8.18, and by the voltage-current relations

$$\left.\begin{aligned} V_1 &= Z_{11}I_1 + Z_{12}I_2 \\ V_2 &= Z_{21}I_1 + Z_{22}I_2 \end{aligned}\right\} \tag{8-63}$$

where

$$Z_{11} = \left.\frac{V_1}{I_1}\right|_{I_2=0} \tag{8-63a}$$

is the input impedance at port #1 with port #2 open-circuited,

$$Z_{12} = \left.\frac{V_1}{I_2}\right|_{I_1=0} \tag{8-63b}$$

(a) Two-port network

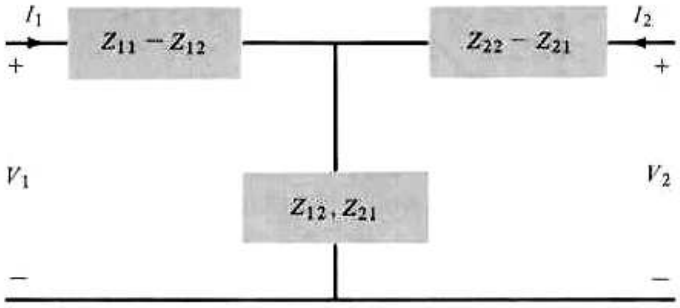

(b) T-network equivalent

Figure 8.18 Two-port network and its T-equivalent.

is the mutual impedance at port #1 due to a current at port #2 (with port #1 open-circuited),

$$Z_{21} = \left.\frac{V_2}{I_1}\right|_{I_2=0} \tag{8-63c}$$

is the mutual impedance at port #2 due to a current in port #1 (with port #2 open-circuited),

$$Z_{22} = \left.\frac{V_2}{I_2}\right|_{I_1=0} \tag{8-63d}$$

is the input impedance at port #2 with port #1 open-circuited. For a reciprocal network, $Z_{12} = Z_{21}$.

The impedances Z_{11} and Z_{22} are the input impedances of antennas 1 and 2, respectively, when each is radiating in an unbounded medium. The presence of another element modifies the input impedance and the extent and nature of the effects depends upon (1) the antenna type, (2) the relative placement of the elements, and (3) the type of feed used to excite the elements.

Equation (8-63) can also be written as

$$Z_{1d} = \frac{V_1}{I_1} = Z_{11} + Z_{12}\left(\frac{I_2}{I_1}\right) \tag{8-64a}$$

$$Z_{2d} = \frac{V_2}{I_2} = Z_{22} + Z_{21}\left(\frac{I_1}{I_2}\right) \tag{8-64b}$$

Z_{1d} and Z_{2d} represent the driving point impedances of antennas 1 and 2, respectively. Each driving point impedance depends upon the current ratio I_1/I_2, the mutual impedance, and the self-input impedance (when radiating into an unbounded medium). When attempting to match any antenna, it is the driving point impedance that must be matched. It is, therefore, apparent that the mutual impedance plays an important role in the performance of an antenna and should be investigated. However, the

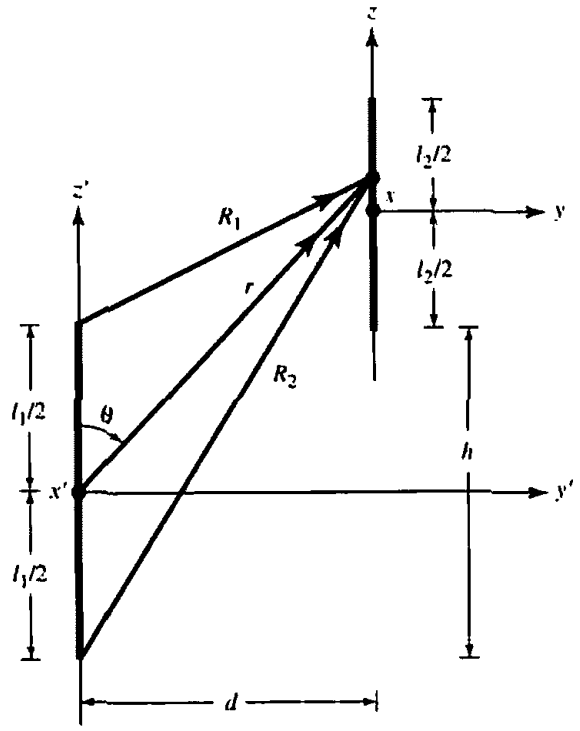

Figure 8.19 Dipole positioning for mutual coupling.

analysis associated with it is usually quite complex and only simplified models can be examined with the induced emf method. Integral Equation-Moment Method techniques can be used for more complex geometries, including skewed arrangements of elements.

Referring to Figure 8.19, the induced open-circuit voltage in antenna 2, *referred to its current at the input terminals*, due to radiation from antenna 1 is given by

$$V_{21} = -\frac{1}{I_{2i}}\int_{-l_2/2}^{l_2/2} E_{z21}(z')I_2(z')\,dz' \tag{8-65}$$

where

$E_{z21}(z')$ = E-field component radiated by antenna 1, which is parallel to antenna 2
$I_2(z')$ = current distribution along antenna 2

Therefore the mutual impedance of (8-63c), (referred to at the *input current* I_{1i} *of antenna 1*), is expressed as

$$Z_{21i} = \frac{V_{21}}{I_{1i}} = -\frac{1}{I_{1i}I_{2i}}\int_{-l_2/2}^{l_2/2} E_{z21}(z')I_2(z')\,dz' \tag{8-66}$$

8.6.1 Integral Equation-Moment Method

To use this method to find the mutual impedance based on (8-66), an integral equation must be formed to find E_{z21}, which is the field radiated by antenna 1 at any point on antenna 2. This integral equation must be a function of the unknown current on antenna 1, and it can be derived using a procedure similar to that used to form Pocklington's Integral Equation of (8-22) or (8-24), or Hallén's Integral Equation of (8-27). The unknown current of antenna 1 can be represented by a series of finite

number of terms with N unknown coefficients and a set of known (chosen) basis functions. The current $I_2(z)$ must also be expanded into a finite series of N terms with N unknown coefficients and a set of N chosen basis functions. Once each of them is formulated, then they can be used interactively to reduce (8-66) into an $N \times N$ set of linearly independent equations to find the mutual impedance.

To accomplish this requires a lengthy formulation, computer programming, and usually a digital computer. The process usually requires numerical integrations or special functions for the evaluation of the impedance matrices of E_{z21} and the integral of (8-66). There are national computer codes, such as the Numerical Electromagnetics Code (NEC) and the simplified version Mini Numerical Electromagnetics Code (MININEC), for the evaluation of the radiation characteristics, including impedances, of wire antennas [35]–[37]. Both of these are based on an Integral Equation-Moment Method formulation. Information concerning these two codes follows. There are other codes; however, these two seem to be the most popular, especially for wire type antennas.

Another procedure that has been suggested to include mutual effects in arrays of linear elements is to use a convergent iterative algorithm [38], [39]. This method can be used in conjunction with a calculator [38], and it has been used to calculate impedances, patterns and directivities of arrays of dipoles [39].

A. Numerical Electromagnetics Code (NEC)

The Numerical Electromagnetics Code (NEC) is a user-oriented program developed at Lawrence Livermore Laboratory. It is a moment method code for analyzing the interaction of electromagnetic waves with arbitrary structures consisting of conducting wires and surfaces. It combines an integral equation for smooth surfaces with one for wires to provide convenient and accurate modeling for a wide range of applications. The code can model nonradiating networks and transmission lines, perfect and imperfect conductors, lumped element loading, and perfect and imperfect conducting ground planes. It uses the electric field integral equation (EFIE) for thin wires and the magnetic field integral equation (MFIE) for surfaces. The excitation can be either an applied voltage source or an incident plane wave. The program computes induced currents and charges, near- and far-zone electric and magnetic fields, radar cross section, impedances or admittances, gain and directivity, power budget, and antenna-to-antenna coupling.

B. Mini-Numerical Electromagnetics Code (MININEC)

The Mini-Numerical Electromagnetics Code (MININEC) [36], [37] is a user-oriented compact version of the NEC developed at the Naval Ocean Systems Center (NOSC). It is also a moment method code, but coded in BASIC, and has retained the most frequently used options of the NEC. It is intended to be used in mini, micro, and personal computers, as well as work stations, and it is most convenient to analyze wire antennas. It computes currents, and near- and far-field patterns. It also optimizes the feed excitation voltages that yield desired radiation patterns.

Information concerning the NEC and MININEC, and their availability, can be directed to:

Professor Richard W. Adler
Naval Postgraduate School
Code 62 AB
Monterey, California 93943

8.6.2 Induced EMF Method

The induced emf method is also based on (8-66) except that $I_2(z')$ is assumed to be the ideal current distribution of (4-56) or (8-58) while $E_{z21}(z')$ is the electric field of (8-55b). Using (8-58) and (8-55b), we can express (8-66) as

$$Z_{21i} = \frac{V_{21}}{I_{1i}} = j\frac{\eta I_{1m} I_{2m}}{4\pi I_{1i} I_{2i}} \int_{-l_2/2}^{l_2/2} \sin\left[k\left(\frac{l_2}{2} - |z'|\right)\right]\left[\frac{e^{-jkR_1}}{R_1} + \frac{e^{-jkR_2}}{R_2} - 2\cos\left(k\frac{l_1}{2}\right)\frac{e^{-jkr}}{r}\right] dz' \tag{8-67}$$

where r, R_1, and R_2 are given, respectively, by (8-53a), (8-53b) and (8-53c) but with $y = d$ and $l = l_1$. I_{1m}, I_{2m} and I_{1i}, I_{2i} represent, respectively, the maximum and input currents for antennas 1 and 2. By referring each of the maximum currents to those at the input using (4-78) and assuming free space, we can write (8-67) as

$$Z_{21i} = j\frac{30}{\sin\left(\frac{kl_1}{2}\right)\sin\left(\frac{kl_2}{2}\right)} \int_{-l_2/2}^{l_2/2} \sin\left[k\left(\frac{l_2}{2} - |z'|\right)\right]\left[\frac{e^{-jkR_1}}{R_1} + \frac{e^{-jkR_2}}{R_2} - 2\cos\left(k\frac{l_1}{2}\right)\frac{e^{-jkr}}{r}\right] dz' \tag{8-68}$$

The mutual impedance referred to the current maxima is related to that at the input of (8-68) by

$$Z_{21m} = Z_{21i} \sin\left(\frac{kl_1}{2}\right)\sin\left(\frac{kl_2}{2}\right) \tag{8-69}$$

which for identical elements ($l_1 = l_2 = l$) reduces to

$$Z_{21m} = Z_{21i} \sin^2\left(\frac{kl}{2}\right) \tag{8-70}$$

whose real and imaginary parts are related by

$$R_{21m} = R_{21i} \sin^2\left(\frac{kl}{2}\right) \tag{8-70a}$$

$$X_{21m} = X_{21i} \sin^2\left(\frac{kl}{2}\right) \tag{8-70b}$$

For a two-element array of linear dipoles, there are three classic configurations for which closed-form solutions for (8-68), in terms of sine and cosine integrals, are obtained [33]. These are shown in Figure 8.20, and they are referred to as the *side-by-side* [Fig. 8.20(a)], *collinear* [Fig. 8.20(b)], and *parallel-in-echelon* [Fig. 8.20(c)]. For two identical elements (each with *odd* multiples of $\lambda/2$, $l = n\lambda/2$, $n = 1, 3, 5, \ldots$) (8-70) reduces for each arrangement to the expressions that follow. Expressions for linear elements of any length are much more complex and can be found in [33].

A computer program referred to as SELF AND MUTUAL IMPEDANCES, based on (8-71a)–(8-73i), is included at the end of the chapter.

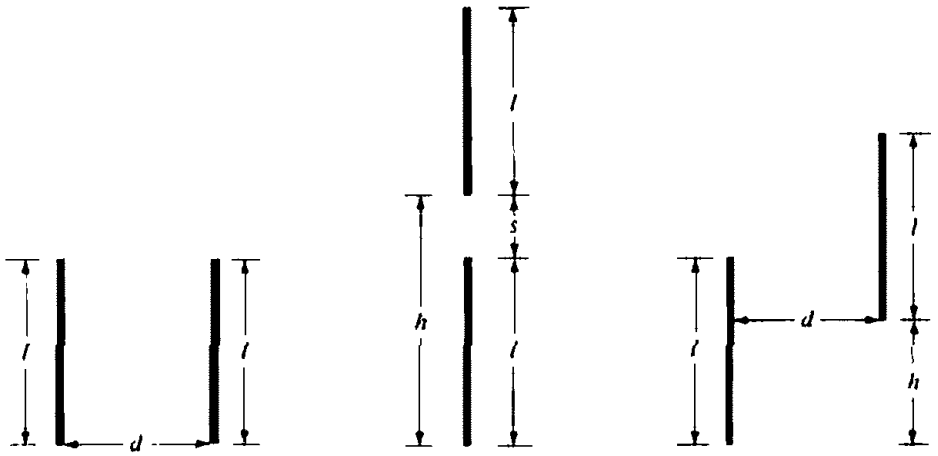

(a) Side-by-side (b) Collinear (c) Parallel in echelon

Figure 8.20 Dipole configuration of two identical elements for mutual impedance computations.

Side-by-Side Configuration [Figure 8.20(a)]

$$R_{21m} = \frac{\eta}{4\pi}[2C_i(u_0) - C_i(u_1) - C_i(u_2)] \tag{8-71a}$$

$$X_{21m} = -\frac{\eta}{4\pi}[2S_i(u_0) - S_i(u_1) - S_i(u_2)] \tag{8-71b}$$

$$u_0 = kd \tag{8-71c}$$

$$u_1 = k(\sqrt{d^2 + l^2} + l) \tag{8-71d}$$

$$u_2 = k(\sqrt{d^2 + l^2} - l) \tag{8-71e}$$

Collinear Configuration [Figure 8.20(b)]

$$R_{21m} = -\frac{\eta}{8\pi}\cos(v_0)[-2C_i(2v_0) + C_i(v_2) + C_i(v_1) - \ln(v_3)] + \frac{\eta}{8\pi}\sin(v_0)[2S_i(2v_0) - S_i(v_2) - S_i(v_1)] \tag{8-72a}$$

$$X_{21m} = -\frac{\eta}{8\pi}\cos(v_0)[2S_i(2v_0) - S_i(v_2) - S_i(v_1)] + \frac{\eta}{8\pi}\sin(v_0)[2C_i(2v_0) - C_i(v_2) - C_i(v_1) - \ln(v_3)] \tag{8-72b}$$

$$v_0 = kh \tag{8-72c}$$

$$v_1 = 2k(h + l) \tag{8-72d}$$

$$v_2 = 2k(h - l) \tag{8-72e}$$

$$v_3 = (h^2 - l^2)/h^2 \tag{8-72f}$$

Parallel-in-Echelon Configuration [Figure 8.20(c)]

$$R_{21m} = -\frac{\eta}{8\pi}\cos(w_0)[-2C_i(w_1) - 2C_i(w_1') + C_i(w_2) + C_i(w_2') + C_i(w_3) + C_i(w_3')] + \frac{\eta}{8\pi}\sin(w_0)[2S_i(w_1) - 2S_i(w_1') - S_i(w_2) + S_i(w_2') - S_i(w_3) + S_i(w_3')] \tag{8-73a}$$

$$X_{21m} = -\frac{\eta}{8\pi}\cos(w_0)[2S_i(w_1) + 2S_i(w_1') - S_i(w_2) - S_i(w_2') - S_i(w_3) - S_i(w_3')] + \frac{\eta}{8\pi}\sin(w_0)[2C_i(w_1) - 2C_i(w_1') - C_i(w_2) + C_i(w_2') - C_i(w_3) + C_i(w_3')] \tag{8-73b}$$

$$w_0 = kh \tag{8-73c}$$

$$w_1 = k(\sqrt{d^2 + h^2} + h) \tag{8-73d}$$

$$w_1' = k(\sqrt{d^2 + h^2} - h) \tag{8-73e}$$

$$w_2 = k[\sqrt{d^2 + (h - l)^2} + (h - l)] \tag{8-73f}$$

$$w_2' = k[\sqrt{d^2 + (h - l)^2} - (h - l)] \tag{8-73g}$$

$$w_3 = k[\sqrt{d^2 + (h + l)^2} + (h + l)] \tag{8-73h}$$

$$w_3' = k[\sqrt{d^2 + (h + l)^2} - (h + l)] \tag{8-73i}$$

The mutual impedance, referred to the current maximum, based on the induced emf method of a side-by-side and a collinear arrangement of two half-wavelength dipoles is shown plotted in Figure 8.21. It is apparent that the side-by-side arrangement exhibits larger mutual effects since the antennas are placed in the direction of maximum radiation. The data is compared with those based on the Moment Method/NEC [35] using a wire with a radius of $10^{-5}\lambda$. A very good agreement is indicated between the two sets because a wire with a radius of $10^{-5}\lambda$ for the MM/NEC is considered very thin. Variations as a function of the radius of the wire for both the side-by-side and collinear arrangements using the MM/NEC are shown, respectively, in Figures 8.22(a,b). Similar sets of data were computed for the parallel-in-echelon arrangement of Figure 8.20(c), and they are shown, respectively, in Figures 8.23(a) and 8.23(b) for $d = \lambda/4$, $0 \le h \le \lambda$ and $h = \lambda/2$, $0 < d < \lambda$ for wire radii of $10^{-5}\lambda$. Again a very good agreement between the induced emf and Moment Method/NEC data is indicated.

Example 8.6

Two identical linear half-wavelength dipoles are placed in a side-by-side arrangement, as shown in Figure 8.20(a). Assuming that the separation between the elements is $d = 0.35\lambda$, find the driving point impedance of each.

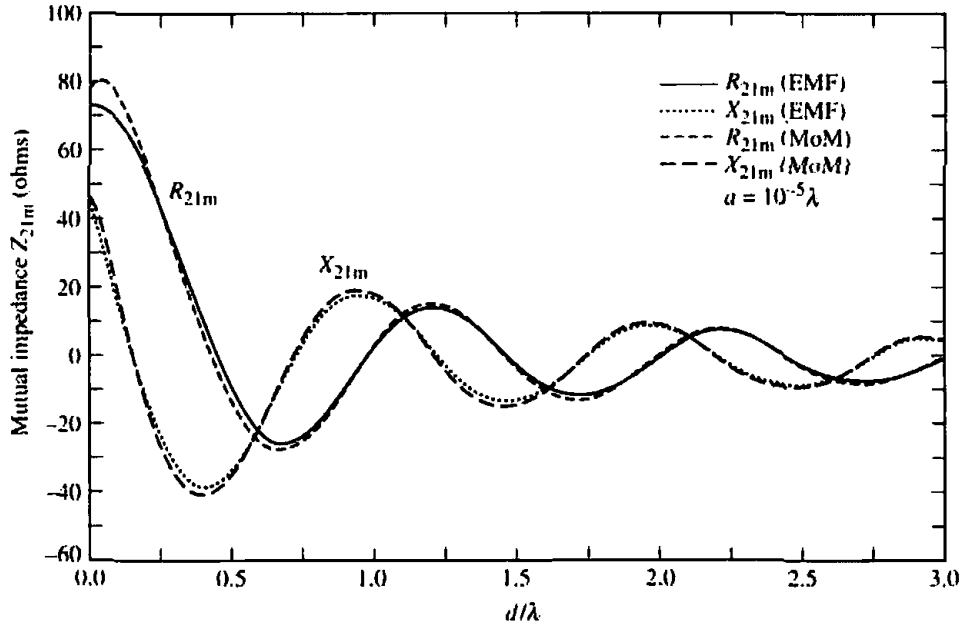

(a) Side-by-side

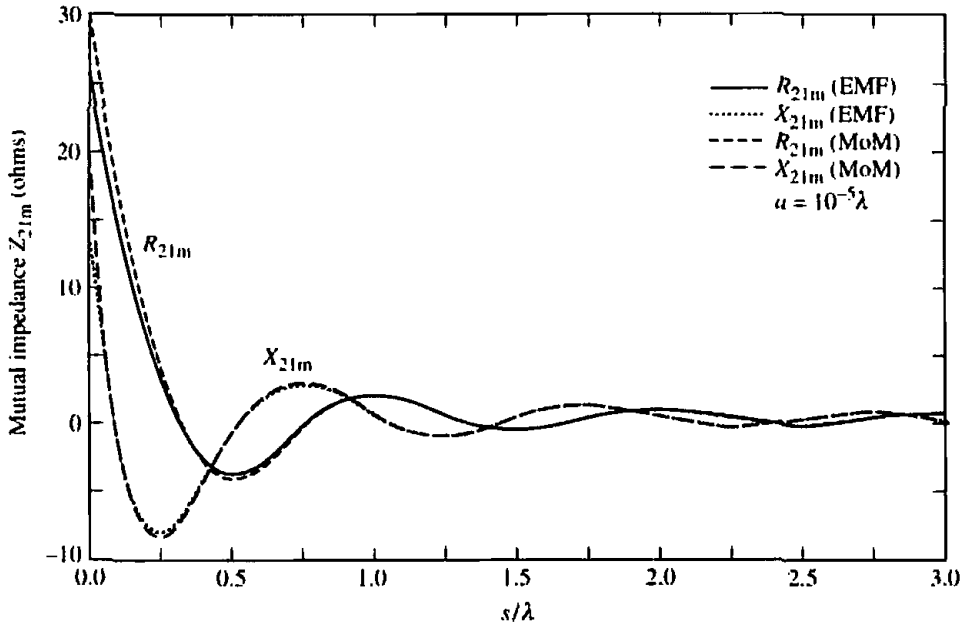

(b) Collinear

Figure 8.21 Mutual impedance of two side-by-side and collinear $\lambda/2$ dipoles using the moment method and induced emf method.

SOLUTION

Using (8-64a)

$$Z_{1d} = \frac{V_1}{I_1} = Z_{11} + Z_{12}\left(\frac{I_2}{I_1}\right)$$

Since the dipoles are identical, $I_1 = I_2$. Thus

$$Z_{1d} = Z_{11} + Z_{12}$$

From Figure 8.21(a)

$$Z_{12} = 25 - j38$$

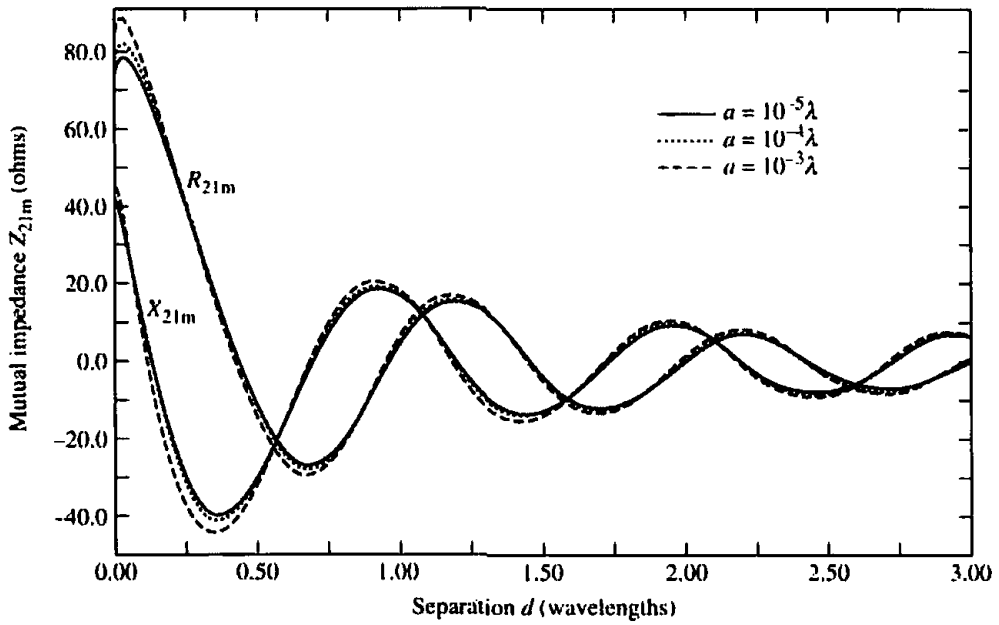

(a) Side-by-side

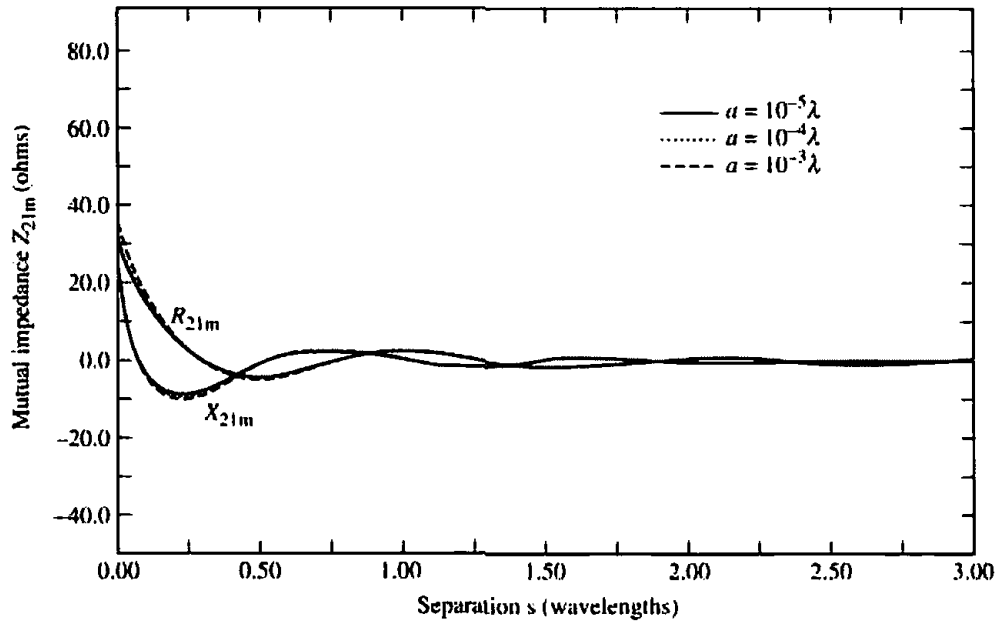

(b) Collinear

Figure 8.22 Variations of mutual impedance as a function of wire radius for side-by-side and collinear $\lambda/2$ dipole arrangements.

Since

$$Z_{11} = 73 + j42.5$$

Z_{1d} reduces to

$$Z_{1d} \simeq 98 + j4.5$$

which is also equal to Z_{2d} of (8-64b).

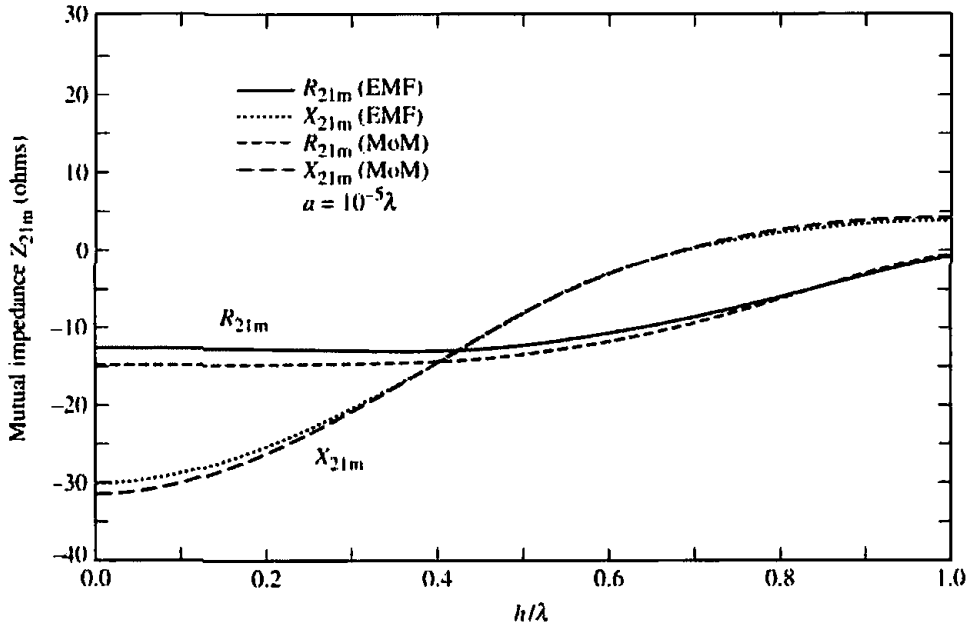

(a) $d = 0.5\lambda$

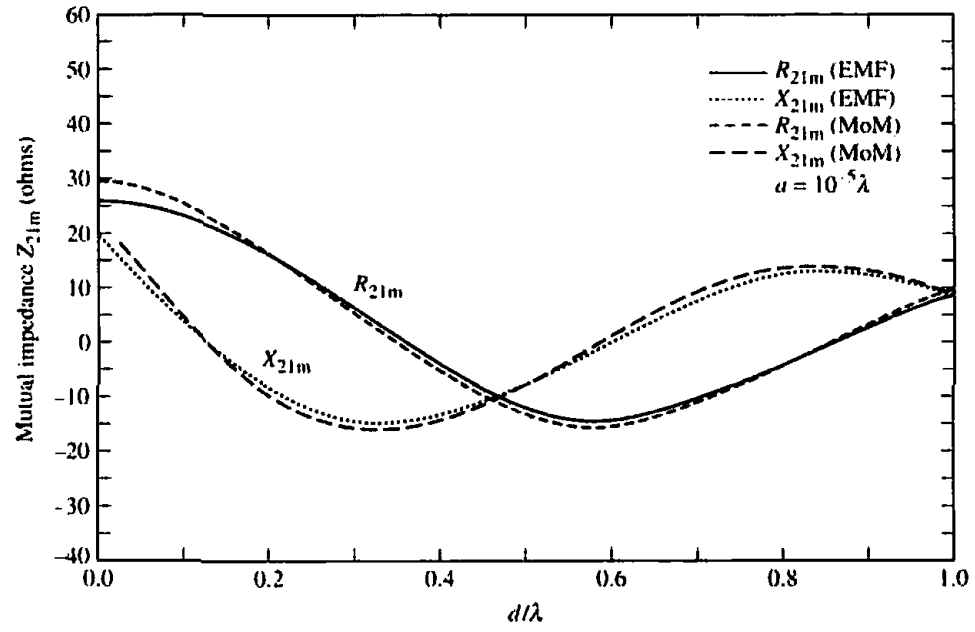

(b) $h = 0.5\lambda$

Figure 8.23 Mutual impedance for two parallel-in-echelon $\lambda/2$ dipoles with wire radii of $10^{-5}\ \lambda$.

As discussed in Chapter 2, Section 2.13, maximum power transfer between the generator and the transmitting antenna occurs when their impedances are conjugate-matched. The same is necessary for the receiver and receiving antenna. This ensures maximum power transfer between the transmitter and receiver, when there is no interaction between the antennas. In practice, the input impedance of one antenna depends on the load connected to the other antenna. Under those conditions, the matched loads and maximum coupling can be computed using the Linville method [40], which is used in rf amplifier design. This technique has been incorporated into the NEC [35]. Using this method, maximum coupling is computed using [35]

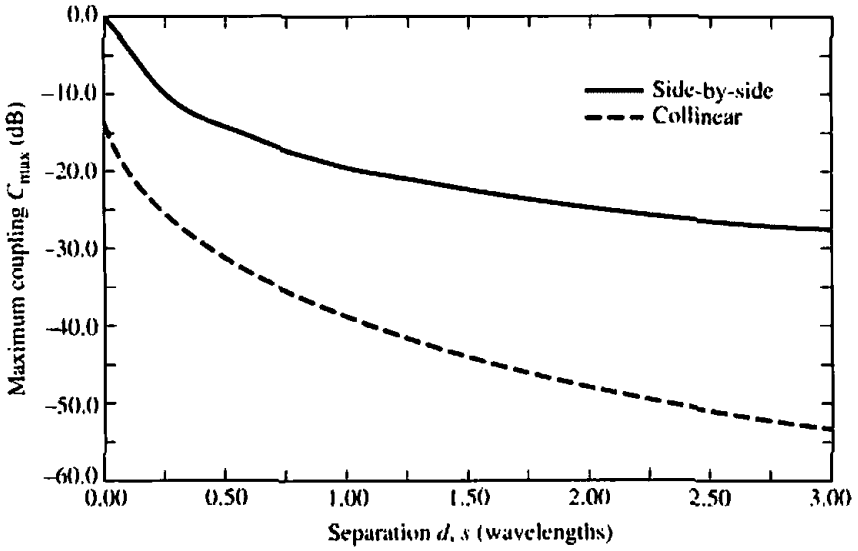

Figure 8.24 Maximum coupling for the two λ/2 dipoles in side-by-side and collinear arrangements as a function of separation.

$$C_{\max} = \frac{1}{L}[1 - (1 - L^2)^{1/2}] \tag{8-74}$$

where

$$L = \frac{|Y_{12}Y_{21}|}{2\text{Re}(Y_{11})\,\text{Re}(Y_{22}) - \text{Re}(Y_{12}Y_{21})} \tag{8-74a}$$

To ensure maximum coupling, the admittance of the matched load on the receiving antenna should be [35]

$$Y_L = \left[\frac{1 - \rho}{1 + \rho} + 1\right]\text{Re}(Y_{22}) - Y_{22} \tag{8-75}$$

where

$$\rho = \frac{G_{\text{MAX}}(Y_{12}Y_{21})^*}{|Y_{12}Y_{21}|} \tag{8-75a}$$

The corresponding input admittance of the transmitting antenna is

$$Y_{\text{in}} = Y_{11} - \frac{Y_{21}Y_{12}}{Y_L + Y_{22}} \tag{8-76}$$

Based on (8-74)–(8-76), maximum coupling for two half-wavelength dipoles in side-by-side and collinear arrangements as a function of the element separation (d for side-by-side and s for collinear) was computed using the NEC, and it is shown in Figure 8.24. As expected, the side-by-side arrangement exhibits much stronger coupling, since the elements are placed along the direction of their respective maximum radiation. Similar curves can be computed for the parallel-in-echelon arrangement.

8.7 MUTUAL COUPLING IN ARRAYS

When two antennas are near each other, whether one and/or both are transmitting or receiving, some of the energy that is primarily intended for one ends up at the other.

The amount depends primarily on the

a. radiation characteristics of each
b. relative separation between them
c. relative orientation of each

There are many different mechanisms that can cause this interchange of energy. For example, even if both antennas are transmitting, some of the energy radiated from each will be received by the other because of the nonideal directional characteristics of practical antennas. Part of the incident energy on one or both antennas may be rescattered in different directions allowing them to behave as secondary transmitters. This interchange of energy is known as "mutual coupling," and in many cases it complicates the analysis and design of an antenna. Furthermore, for most practical configurations, mutual coupling is difficult to predict analytically but must be taken into account because of its significant contribution. Because the mutual effects of any antenna configuration cannot be generalized, in this section we want first to briefly introduce them in a qualitative manner and then examine their general influence on the behavior of the radiation characteristics of the antenna. Most of the material and presentation in this section is followed from a well-written document on this subject [41].

8.7.1 Coupling in the Transmitting Mode

To simplify the discussion, let us assume that two antennas m and n of an array are positioned relative to each other as shown in Figure 8.25(a). The procedure can be extended to a number of elements. If a source is attached to antenna n, the generated energy traveling toward the antenna labeled as (0) will be radiated into space (1) and toward the mth antenna (2). The energy incident on the mth antenna sets up currents which have a tendency to rescatter some of the energy (3) and allow the remaining to travel toward the generator of m (4). Some of the rescattered energy (3) may be redirected back toward antenna n (5). This process can continue indefinitely. The same process would take place if antenna m is excited and antenna n is the parasitic element. If both antennas, m and n, are excited simultaneously, the radiated and rescattered fields by and from each must be added vectorially to arrive at the total field at any observation point. Thus, "*the total contribution to the far-field pattern of a particular element in the array depends not only upon the excitation furnished by its own generator (the direct excitation) but upon the total parasitic excitation as well, which depends upon the couplings from and the excitation of the other generators* [41]."

The wave directed from the n to the m antenna and finally toward its generator (4) adds vectorially to the incident and reflected waves of the m antenna itself, thus enhancing the existing standing wave pattern within m. For coherent excitations, the coupled wave (4) due to source n differs from the reflected one in m only in phase and amplitude. The manner in which these two waves interact depends on the coupling between them and the excitation of each. It is evident then that the vector sum of these two waves will influence the input impedance looking in at the terminals of antenna m and will be a function of the position and excitation of antenna n. This coupling effect is commonly modeled as a change in the apparent driving impedance of the elements and it is usually referred to as *mutual impedance variation.*

To demonstrate the usefulness of the driving impedance variation, let us assume

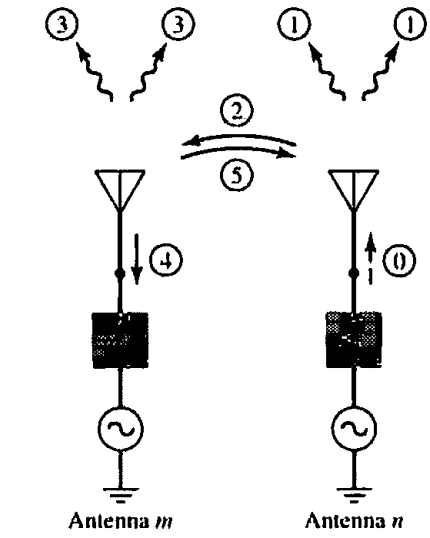

(a) Transmitting

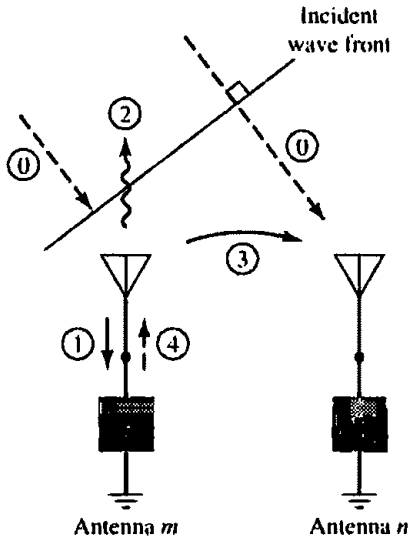

(b) Receiving

Figure 8.25 Transmitting mode coupling paths between antennas m and n (Reprinted with permission of MIT Lincoln Laboratory, Lexington, MA).

that a set of elements in an array are excited. For a given element in the array, the generator impedance that is optimum in the sense of maximizing the radiated power for that element is that which would be a conjugate impedance match at the element terminals. This is accomplished by setting a reflected wave which is equal in amplitude and phase to the backwards traveling waves induced due to the coupling. Even though this is not the generator impedance which is a match to a given element when all other elements are not excited, it does achieve maximum power transfer.

To minimize confusion, let us adopt the following terminology [41]:

1. *Antenna impedance:* The impedance looking into a single isolated element.
2. *Passive driving impedance:* The impedance looking into a single element of an array with all other elements of the array passively terminated in their normal generator impedance unless otherwise specified.
3. *Active driving impedance:* The impedance looking into a single element of an array with all other elements of the array excited.

Since the passive driving impedance is of minor practical importance and differs only slightly from the antenna impedance, the term *driving impedance* will be used to indicate *active* driving impedance, unless otherwise specified.

Since the driving impedance for a given element is a function of the placement and excitation of the other elements, then *optimum generator impedance that maximizes array radiation efficiency (gain) varies with array excitation.* These changes, with element excitation variations, constitute one of the principal aggravations in electronic scanning arrays.

8.7.2 Coupling in the Receiving Mode

To illustrate the coupling mechanism in the receiving mode, let us again assume that the antenna system consists of two passively loaded elements of a large number, as shown in Figure 8.25(b). Assume that a plane wave (0) is incident, and it strikes antenna *m* first where it causes current flow. Part of the incident wave will be rescattered into space as (2), the other will be directed toward antenna *n* as (3) where it will add vectorially with the incident wave (0), and part will travel into its feed as (1). It is then evident that the amount of energy received by each element of an antenna array is the vector sum of the direct waves and those that are coupled to it parasitically from the other elements.

The amount of energy that is absorbed and reradiated by each element depends on its match to its terminating impedance. Thus, the amount of energy received by any element depends upon its terminating impedance as well as that of the other elements. In order to maximize the amount of energy extracted from an incident wave, we like to minimize the total backscattered (2) energy into space by properly choosing the terminating impedance. This actually can be accomplished by mismatching the receiver itself relative to the antenna so that the reflected wave back to the antenna (4) is cancelled by the rescattered wave, had the receiver been matched to the actual impedance of each antenna.

As a result of the previous discussion, it is evident that mutual coupling plays an important role in the performance of an antenna. However, the analysis and understanding of it may not be that simple.

8.7.3 Mutual Coupling on Array Performance

The effects of the mutual coupling on the performance of an array depends upon the

a. antenna type and its design parameters
b. relative positioning of the elements in the array
c. feed of the array elements
d. scan volume of the array

These design parameters influence the performance of the antenna array by varying its element impedance, reflection coefficients, and overall antenna pattern. In a finite-element array, the multipath routes the energy follows because of mutual coupling will alter the pattern in the absence of these interactions. However, for a very large regular array (array with elements placed at regular intervals on a grid and of sufficient numbers so that edge effects can be ignored), the relative shape of the pattern will be the same with and without coupling interactions. It will only require a scaling up or down in amplitude while preserving the shape. This, however, is not true for irregular placed elements or for small regular arrays where edge effects become dominant.

8.7.4 Coupling in an Infinite Regular Array

The analysis and understanding of coupling can be considerably simplified by considering an infinite regular array. Although such an array is not physically realizable, it does provide an insight and in many cases answers of practical importance. For the infinite regular array we assume that

a. all the elements are placed at regular intervals
b. all the elements are identical
c. all the elements have uniform (equal) amplitude excitation
d. there can be a linear relative phasing between the elements in the two orthogonal directions

The geometry of such an array is shown in Figure 6.23 with its array factor given by (6-87) or (6-88). This simplified model will be used to analyze the coupling and describes fairly accurately the behavior of most elements in arrays of modest to large size placed on flat or slowly curve surfaces with smoothly varying amplitude and phase taper.

To assess the behavior of the element driving impedance as a function of scan angle, we can write the terminal voltage of any one element in terms of the currents flowing in the others, assuming a single-mode operation, as

$$V_{mn} = \sum_{p} \sum_{q} Z_{mn,pq} I_{pq} \tag{8-77}$$

where $Z_{mn,pq}$ defines the terminal voltage at antenna mn due to a unity current in element pq when the current in all the other elements is zero. Thus the $Z_{mn,pq}$ terms represent the *mutual impedances* when the indices mn and pq are not identical. The *driving impedance* of the mnth element is defined as

$$Z_{Dmn} = \frac{V_{mn}}{I_{mn}} = \sum_{p} \sum_{q} Z_{mn,pq} \frac{I_{pq}}{I_{mn}} \tag{8-78}$$

Since we assumed that the amplitude excitation of the elements of the array was uniform and the phase linear, we can write that

$$I_{pq} = I_{00} e^{j(p\beta_x + q\beta_y)} \tag{8-79a}$$

$$I_{mn} = I_{00} e^{j(m\beta_x + n\beta_y)} \tag{8-79b}$$

Thus, (8-78) reduces to

$$Z_{Dmn} = \sum_{p} \sum_{q} Z_{mn,pq} e^{j(p-m)\beta_x} e^{j(q-n)\beta_y} \tag{8-80}$$

It is evident that the driving point impedance of mn element is equal to the vector sum of the element self impedance ($mn = pq$) and the phased mutual impedances between it and the other elements ($mn \neq pq$). The element self impedance ($mn = pq$) is obtained when all other elements are open-circuited so that the current at their feed points is zero [$I_{pq}(pq \neq mn) = 0$]. For most practical antennas, physically this is almost equivalent to removing the pq elements and finding the impedance of a single isolated element.

A consequence of the mutual coupling problem is the change of the array impedance with scan angle. In order not to obscure the basic principle with the complexity of the problem, this can best be illustrated by examining the behavior of the reflection

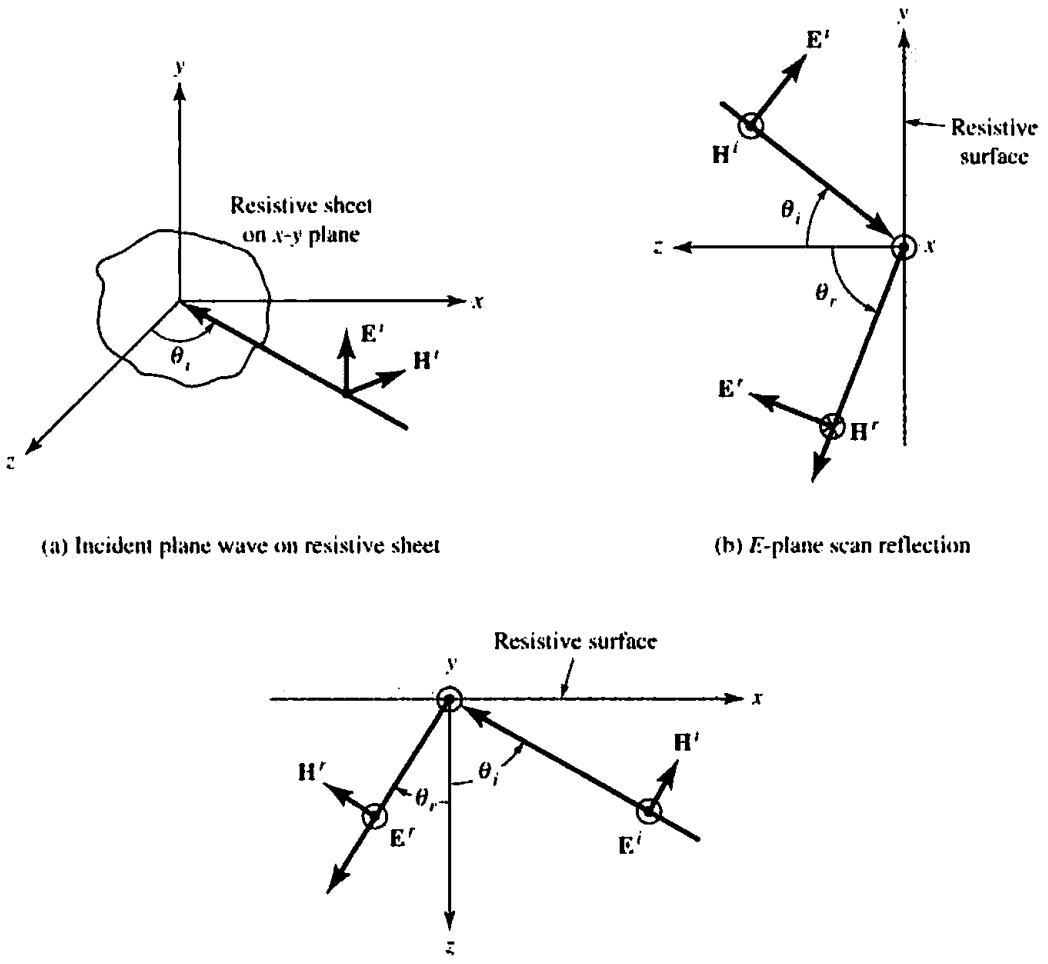

(a) Incident plane wave on resistive sheet

(b) E-plane scan reflection

(c) H-plane scan reflection

Figure 8.26 Geometry for plane wave reflection from resistive sheet. (Reprinted with permission of MIT Lincoln Laboratory, Lexington, MA.)

coefficient of a uniform plane wave in free-space incident on a resistive sheet of infinite extent backed by an open circuit so that there are no transmitted fields through the sheet, as shown in Figure 8.26(a). Although the open circuit is not physically realizable, nevertheless the model is useful. This is accomplished by choosing the surface resistivity of the sheet to be that of free-space ($\eta_0 = 120\pi$) so that the sheet is an exact match for a normally incident wave. Referring to Figure 8.26(b) for an E-plane scan and Figure 8.26(c) for an H-plane scan, we impose that at the boundary ($z = 0$ for all x and y) the ratio of the total tangential electric field to the total tangential magnetic field is equal to the surface impedance of the sheet. The same procedure is used in electromagnetics to derive the Fresnel reflection and transmission coefficients from planar interfaces for vertical and horizontal polarizations [14].

Referring to Figure 8.26(b), we can write that the incident and reflected waves for the **E**- and **H**-fields as

$$\mathbf{E}^i = E_0^i(\hat{\mathbf{a}}_y \cos\theta_i - \hat{\mathbf{a}}_z \sin\theta_i)e^{+jk_0(y\sin\theta_i + z\cos\theta_i)} \tag{8-81a}$$

$$\mathbf{H}^i = \hat{\mathbf{a}}_x H_0^i e^{+jk_0(y\sin\theta_i + z\cos\theta_i)} \tag{8-81b}$$

$$\mathbf{E}^r = E_0^r(\hat{\mathbf{a}}_y \cos\theta_r + \hat{\mathbf{a}}_z \sin\theta_r)e^{-jk_0(-y\sin\theta_r + z\cos\theta_r)} \tag{8-81c}$$

$$\mathbf{H}^r = -\hat{\mathbf{a}}_x H_0^r e^{-jk_0(-y\sin\theta_r + z\cos\theta_r)} \tag{8-81d}$$

Applying boundary conditions on the tangential components of the electric and magnetic field of (8-81a)–(8-81d) gives

$$\eta_0 = \frac{E_{\tan}}{H_{\tan}} = \frac{E_0^i \cos\theta_i e^{jk_0 y \sin\theta_i} + E_0^r \cos\theta_r e^{jk_0 y \sin\theta_r}}{H_0^i e^{jk_0 y \sin\theta_i} - H_0^r e^{jk_0 y \sin\theta_r}} \tag{8-82}$$

Since

$$H_0^i = \frac{E_0^i}{\eta_0} \tag{8-82a}$$

$$H_0^r = \frac{E_0^r}{\eta_0} \tag{8-82b}$$

we can write (8-82) as

$$E_0^i(\cos\theta_i - 1)e^{jk_0 y \sin\theta_i} = -E_0^r(\cos\theta_r + 1)e^{jk_0 y \sin\theta_r} \tag{8-83}$$

whose only solution independent of y occurs when $\theta_r = \theta_i$. Thus,

$$\Gamma_e = \frac{E_0^r}{E_0^i} = \frac{1 - \cos\theta_i}{1 + \cos\theta_i} = \tan^2\left(\frac{\theta_i}{2}\right) \tag{8-84}$$

which can also be written as

$$\Gamma_e = \frac{E_0^r}{E_0^i} = \frac{1 - \cos\theta_i}{1 + \cos\theta_i} = \frac{\dfrac{1}{\cos\theta_i} - 1}{\dfrac{1}{\cos\theta_i} + 1} = \frac{Z_e - 1}{Z_e + 1} \tag{8-85}$$

By comparison with the reflection coefficient Γ of a transmission line with a normalized load $\bar{Z}_L$

$$\Gamma = \frac{\bar{Z}_L - 1}{\bar{Z}_L + 1} \tag{8-86}$$

the sheet represents an impedance to the wave that varies as

$$Z_e = \frac{1}{\cos\theta_i} \tag{8-87}$$

This is usually referred to as a *normalized directional impedance.*

Referring to Figure 8.26(c), it can be shown that for the H-plane scan the reflection coefficient is

$$\Gamma_h = -\frac{1 - \cos\theta_i}{1 + \cos\theta_i} = -\tan^2\left(\frac{\theta_i}{2}\right) \tag{8-88}$$

and the sheet represents to the wave an impedance that varies as

$$Z_h = \cos\theta_i \tag{8-89}$$

It is clear that even for such a simple problem of a plane wave impinging on a resistive sheet, there is a change, as a function of the scan angle, of the apparent impedance that the resistive sheet represents to the wave.

To illustrate the practical importance of the resistive sheet problem, the computed reflection coefficient magnitude for the E- and H-plane scans for arrays of half-

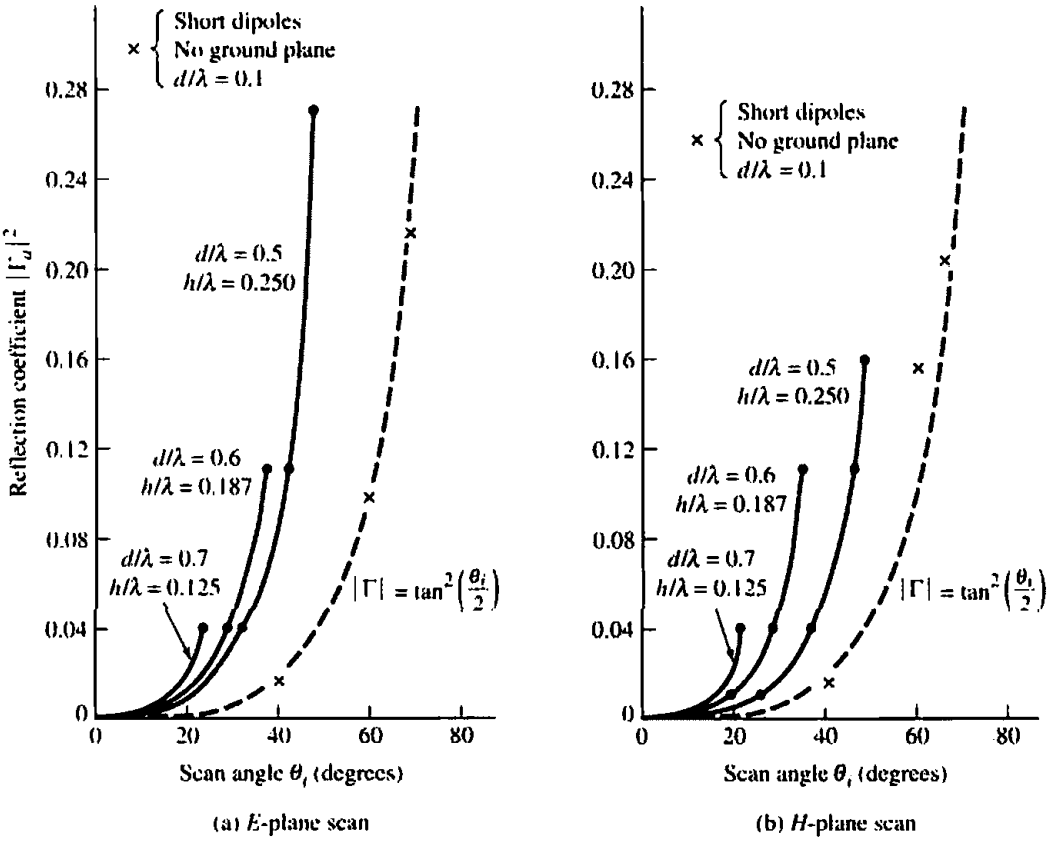

Figure 8.27 Magnitude of reflection coefficient as a function of principal plane scan angle. (Reprinted with permission of MIT Lincoln Laboratory, Lexington, MA.)

wavelength dipoles for various spacings $d(d = d_x = d_y)$ and height h above a ground plane are shown in Figures 8.27(a,b) [41]. The height h was chosen to minimize the mismatch in the principal planes of scan. The curves are discontinued at the angles where major lobes are equally disposed about broadside and retrace themselves beyond that point. The angles of discontinuity become smaller for wider spacings. It is also evident that the reflection coefficient for a given scan angle in the principal plane becomes smaller as the elements are brought closer together. In the same figures and indicated by small x's is the reflection coefficient of the central element of a large array of short dipoles with a spacing of $d_x = d_y = 0.1\lambda$ but without a ground plane. The resistive sheet reflection coefficient is also plotted for comparison purposes. It should be noted that the results of Figure 8.27 were computed assuming the generator impedance is matched to the element driving impedance when the array's major lobe was toward broadside. This requires the tuning of the driving reactance for broadside conditions, which for small spacings is exceedingly large.

8.7.5 Grating Lobes Considerations

Because of the periodic nature of an infinite array, the impedance behavior as a function of scan volume for different elements and interelement spacing can be described in the form of an infinite series. This is accomplished by expressing the radiated and stored (real and reactive) powers in the vicinity of the array in terms of the current, field distribution or pattern, of a typical element. The analysis, which was pioneered by Wheeler [42]; Edelberg and Oliner [43], [44]; and Stark [45] is straightforward, but it will not be included here because it requires a knowledge of Fourier

transforms, and it is beyond the scope of the book at this point. However, some qualitative results will be briefly discussed.

It was shown in Section 6.10.1 that *grating lobes* in an array can be formed provided (6-89a) and (6-89b) are satisfied. This was illustrated by the three-dimensional pattern of Figure 6.29. It was indicated there that additional grating lobes can be formed by increasing the interelement spacing. The grating lobes disappear as the spacing recedes toward zero. In general, grating lobes can be moved into and out of the visible region by controlling the spacing and/or relative phase between the elements.

The dependence of the element driving impedance $Z_D(\beta_x, \beta_y)$ on the pointing direction (scan) of the main beam of the array is demonstrated by examining it for different elements, spacings, and the presence of a ground plane. The discussion is restricted to planar arrays and the impedance variations are illustrated for the *E*-, *H*-, and *D*-planes. We define *D*- as the diagonal plane (45° from the *E*- and *H*-planes) and θ_e, θ_h, and θ_d as the angles of the main beam from broadside for the *E*-, *H*- and *D*-planes, respectively.

If the elements are polarized in the y-direction, then according to (6-90a) and (6-90b) the progressive phase shifts between the elements must be

$$\begin{aligned} \beta_x &= 0 \\ \beta_y &= -kd_y \sin\theta_e \end{aligned} \qquad E\text{-plane scan } (\phi_0 = 90°,\ \theta_0 = \theta_e) \tag{8-90}$$

$$\begin{aligned} \beta_x &= -kd_x \sin\theta_h \\ \beta_y &= 0 \end{aligned} \qquad H\text{-plane scan } (\phi_0 = 0°,\ \theta_0 = \theta_h) \tag{8-91}$$

$$\left(\frac{\beta_x}{d_x}\right)^2 + \left(\frac{\beta_y}{d_y}\right)^2 = k \sin\theta_d \qquad D\text{-plane scan } (\phi_0 = 45°,\ \theta_0 = \theta_d) \tag{8-92}$$

To make the presentation of the results more uniform, the element driving impedance $Z_D(\theta)$ is displayed on a Smith chart in a normalized form

$$Z_D(\theta)_{\text{norm}} = \frac{Z_D(\theta) - jX_D(0)}{R_D(0)} \tag{8-93}$$

where

$$Z_D(\theta) = R_D(\theta) + jX_D(\theta) \tag{8-93a}$$

$$\begin{aligned} R_D(0) &= R_D(\theta = 0°) \\ X_D(0) &= X_D(\theta = 0°) \end{aligned} \qquad \text{beam pointed at broadside} \tag{8-93b}$$

In Figure 8.28, we display the normalized driving impedance in the *E*-, *H*- and *D*-planes for a planar array of half-wavelength dipoles ($l = 0.5\lambda$) spaced $d_x = d_y = 0.55\lambda$ [41]. The *E*- and *H*-planes are discontinued at 65°. Physically that angle corresponds to a grating lobe at $-65°$, symmetrically disposed relative to the main beam. Scanning beyond that point is equivalent to moving the main beam in from 65° or retracing the curve.

For a VSWR of 3:1, the half-wavelength dipole array of Figure 8.28 can be scanned up to 45° in the *H*-plane, 79° in the *D*-plane, and anywhere in the *E*-plane; for a VSWR of 2:1, then the maximum scan angles are 50° in the *E*-plane, 40° in the *H*-plane, and 77° in the *D*-plane. For a small dipole ($l = 0.1\lambda$) the maximum scans are 47° in the *H*-plane, 79° in the *D*-plane, and anywhere for the *E*-plane for a 3:1

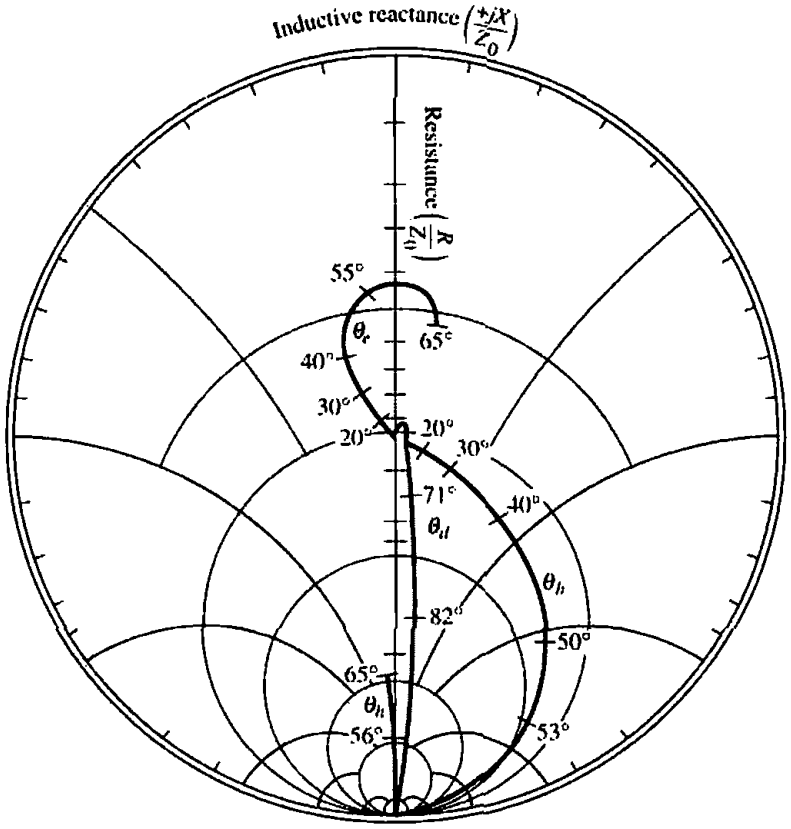

Figure 8.28 Normalized element impedance versus scan angle on the *E*-, *H*-, and *D*-planes for a planar array of half-wavelength dipoles ($l = 0.5\lambda$) with $d_x = d_y = 0.55\lambda$ and with no ground plane. (Reprinted with permission of MIT Lincoln Laboratory, Lexington, MA.)

VSWR; maximum scans of 40° in the *H*-plane, 76° in the *D*-plane, and anywhere in the *E*-plane for a 2:1 VSWR. The results are summarized in Table 8.3 [41].

To demonstrate the effects of a ground plane on the element driving impedance, the normalized impedance of the half-wavelength ($l = 0.5\lambda$) dipole arrays, when placed horizontally a height $h = 0.25\lambda$ above an infinite electric ground plane, are displayed in Figure 8.29. Physically, the introduction of the ground plane below the

Table 8.3 MAXIMUM SCAN VOLUME OF SHORT AND HALF-WAVELENGTH DIPOLE PLANAR ARRAY WITH $d_x = d_y = 0.55\lambda$ AND WITHOUT GROUND PLANE FOR VSWRs OF 3:1 AND 2:1
[Reprinted with permission of MIT Lincoln Laboratory, Lexington, MA]

		Maximum Scan Angle	
VSWR	Scan Plane	Short Dipole ($l = 0.1\lambda$)	Half-Wavelength Dipole ($l = 0.5\lambda$)
3:1	*E*-Plane	—	—
	H-Plane	47°	45°
	D-Plane	79°	79°
2:1	*E*-Plane	—	50°
	H-Plane	40°	40°
	D-Plane	76°	77°

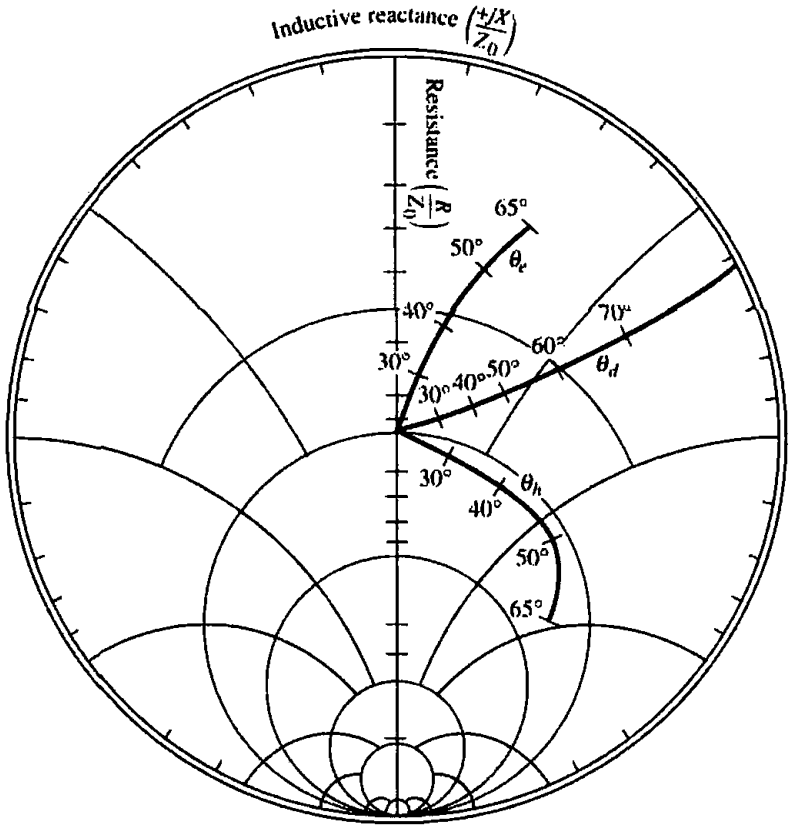

Figure 8.29 Normalized element impedance versus scan angle on the *E*-, *H*-, and *D*-planes for a planar array of half-wavelength ($\ell = 0.5\lambda$) dipoles with $d_x = d_y = 0.55\lambda$ and placed $h = 0.25\lambda$ above a ground plane. (Reprinted with permission of MIT Lincoln Laboratory, Lexington, MA.)

horizontal electric dipoles prevents them from radiating along the ground plane, so the impedance is continuous when a grating lobe moves into the visible region. The maximum scan angles for VSWR's of 3:1 and 2:1 are shown listed in Table 8.4 [41].

The impedances of a short dipole ($l = 0.1\lambda$) are similar to those of the half-wavelength dipole shown in Figures 8.28 and 8.29. The most striking variation in

Table 8.4 MAXIMUM SCAN VOLUME OF SHORT AND HALF-WAVELENGTH DIPOLE PLANAR ARRAY WITH $d_x = d_y = 0.55\lambda$ AND WITH GROUND PLANE ($h = 0.25\lambda$) FOR VSWRs OF 3:1 AND 2:1
[Reprinted with permission of MIT Lincoln Laboratory, Lexington, MA]

		Maximum Scan Angle	
VSWR	Scan Plane	Short Dipole ($l = 0.1\lambda$)	Half-Wavelength Dipole ($l = 0.5\lambda$)
3:1	*E*-Plane	55°	50°
	H-Plane	50°	50°
	D-Plane	62°	62°
2:1	*E*-Plane	45°	40°
	H-Plane	40°	40°
	D-Plane	52°	50°

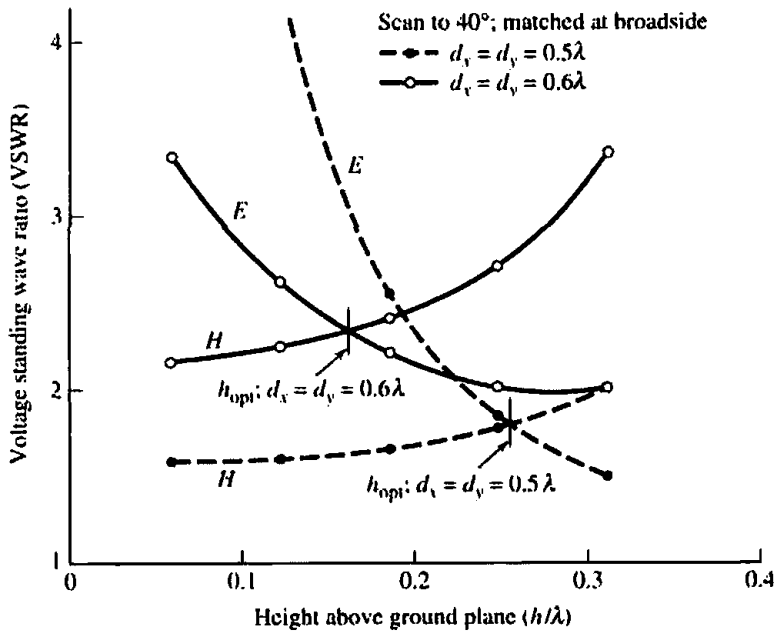

Figure 8.30 VSWR at θ_{max} versus height above ground plane for two large planar square arrays of half-wavelength ($\ell = 0.5\lambda$) dipoles. (Reprinted with permission of MIT Lincoln Laboratory, Lexington, MA.)

impedance of a given array of dipoles is accomplished by the introduction of the ground plane particularly for scan angles near grating-lobe formation.

By comparing the results of Tables 8.3 and 8.4 it is evident that if for dipole arrays the element spacing for allowing grating lobes to appear marginally is used as a design criterion, placing the arrays above a ground plane would give vastly better (but still poor) VSWR performance at extreme scans. If, however, the element spacing is chosen to maintain the maximum VSWR below a given value, there appears little difference between the elements but results in a smaller maximum scan for a given element spacing.

To examine the effect the height h above the ground plane has on the maximum VSWR (within a specified scan volume), the maximum VSWR as a function of the height for E- and H-plane scans of two large square arrays of half-wavelength dipoles with $d_x = d_y = 0.5\lambda$ and $d_x = d_y = 0.6\lambda$ spacing between the elements are displayed in Figure 8.30. The maximum scan angle is 40° and the arrays are assumed to be matched at broadside. It is evident from the results that as the height is decreased the maximum E-plane mismatch becomes very large while that of the H-plane decreases monotonically. The optimum height which leads to equal maximum mismatches in the E- and H-planes of scan for a given scan volume is determined by the spacing between the elements. The optimum heights for the two arrays are indicated in Figure 8.30.

It can be concluded that when an array is placed at its optimum height above the ground plane for a given scan volume and the spacing between the elements of the array is smaller than that required by the grating lobes, that array will exhibit less impedance variations than the one which just satisfies the scan volume requirement.

To demonstrate the variations of the input reflection coefficient, and thus of the input impedance, of an infinite array as a function of scan angle, the input reflection coefficient of an infinite array of circular microstrip patches matched at broadside is shown in Figure 8.31 for the E-plane and H-plane [46]. The variations are due mainly to coupling between the elements. The variations are more pronounced for the

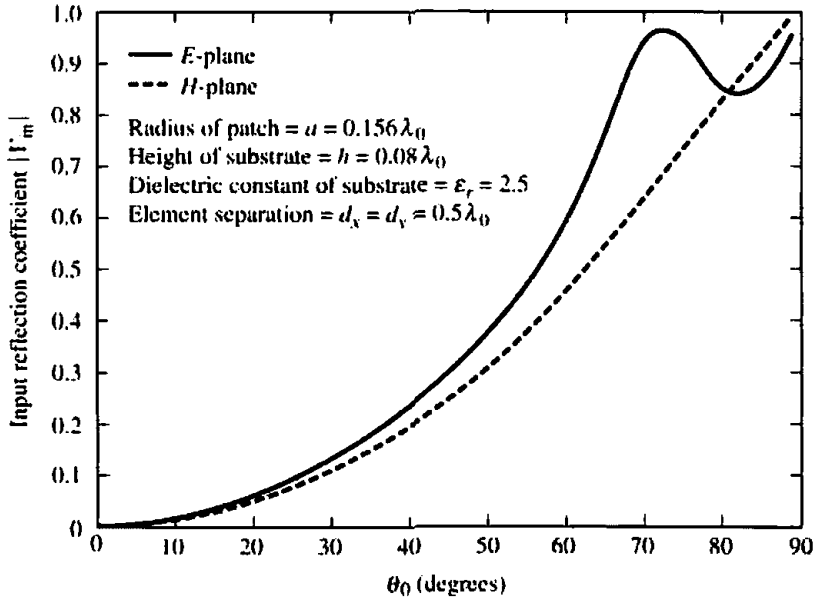

Figure 8.31 Typical magnitude of input reflection coefficient versus scan angle in *E*- and *H*-planes for infinite array of microstrip patches (courtesy J. T. Aberle and F. Zavosh).

E-plane than for the *H*-plane. For microstrip patches, coupling is attributed to space waves (with $1/r$ radial variations), higher order waves (with $1/\rho^2$ radial variations), surface waves (with $1/\rho^2$ radial variations), and leaky waves [with $\exp(-\lambda\rho)/\rho^{1/2}$ radial variations]. As is shown in Chapter 14 and Figures 14.36, 14.37, the variations of the reflection coefficient can be reduced by suppressing the surface waves supported by the substrate using cavities to back the patches [46]. The variations of the reflection coefficient as a function of scan angle can lead, due to large values of the reflection coefficient (ideally unity), to what is usually referred as *array scan blindness* [47]–[50]. This is evident for the *E*-plane near 72°–73° and is due to excitation in that plane of a leaky-wave mode, which is not as strongly excited as the scan angle increases beyond those values. Scan blindness is reached at a scan angle of 90°. Also there can be degradation of side lobe level and main beam shape due to the large variations of the reflection coefficient.

Scan blindness is attributed to slow waves which are supported by the structure of the antenna array. These structures may take the form of dielectric layers (such as radomes, superstrates and substrates) over the face of the array, or metallic grids or fence structures. The scan blindness has been referred to as a "forced surface wave" [47], [48], or a "leaky wave" [49], resonant response of the slow wave structure by the phased array. For the microstrip arrays, the substrate layer supports a slow surface wave which contributes to scan blindness [50].

References

1. R. E. Burgess, "Aerial Characteristics," *Wireless Engr.*, Vol. 21, pp. 154–160, April 1944.
2. J. D. Kraus, *Antennas*, McGraw-Hill, New York, 1988, Chapters 9, 10, pp. 359–434.
3. S. A. Schelkunoff and H. T. Friis, *Antennas: Theory and Practice*, Wiley, New York, 1952, pp. 213–242.
4. A. A. Pistolkors, "The Radiation Resistance of Beam Antennas," *Proc. IRE*, Vol. 17, pp. 562–579, March 1929.
5. R. Bechmann, "On the Calculation of Radiation Resistance of Antennas and Antenna Combinations," *Proc. IRE*, Vol. 19, pp. 461–466, March 1931.

6. P. S. Carter, "Circuit Relations in Radiation Systems and Applications to Antenna Problems." *Proc. IRE*, Vol. 20, pp. 1004–1041, June 1932.
7. R. F. Harrington, "Matrix Methods for Field Problems," *Proc. IEEE*, Vol. 55, No. 2, pp. 136–149, February 1967.
8. R. F. Harrington, *Field Computation by Moment Methods*, Macmillan, New York, 1968.
9. J. H. Richmond, "Digital Computer Solutions of the Rigorous Equations for Scattering Problems," *Proc. IEEE*, Vol. 53, pp. 796–804, August 1965.
10. L. L. Tsai, "Moment Methods in Electromagnetics for Undergraduates," *IEEE Trans. on Education*, Vol. E-21, No. 1, pp. 14–22, February 1978.
11. R. Mittra (Ed.), *Computer Techniques for Electromagnetics*, Pergamon, New York, 1973.
12. J. Moore and R. Pizer, *Moment Methods in Electromagnetics*, John Wiley and Sons, New York, 1984.
13. J. J. H. Wang, *Generalized Moment Methods in Electromagnetics*, John Wiley and Sons, New York, 1991.
14. C. A. Balanis, *Advanced Engineering Electromagnetics*, John Wiley and Sons, New York, 1989.
15. J. D. Lilly, "Application of The Moment Method to Antenna Analysis," MSEE Thesis, Department of Electrical Engineering, West Virginia University, 1980.
16. J. D. Lilly and C. A. Balanis, "Current Distributions, Input Impedances, and Radiation Patterns of Wire Antennas," North American Radio Science Meeting of URSI, Université Laval, Quebec, Canada, June 2–6, 1980.
17. D. K. Cheng, *Field and Wave Electromagnetics*, Addison-Wesley, Reading, MA, 1989, p. 97.
18. H. C. Pocklington, "Electrical Oscillations in Wire," *Cambridge Philos. Soc. Proc.*, Vol. 9, pp. 324–332, 1897.
19. E. Hallén, "Theoretical investigations into the transmitting and receiving qualities of antennae," *Nova Acta Regiae Soc. Sci. Upsaliensis*, Ser. IV, No. 4, pp. 1–44, 1938.
20. R. King and C. W. Harrison, Jr., "The distribution of current along a symmetric center-driven antenna," *Proc. IRE*, Vol. 31, pp. 548–567, October 1943.
21. J. H. Richmond, "A Wire-Grid Model for Scattering by Conducting Bodies," *IEEE Trans. Antennas Propagat.*, Vol. AP-14, No. 6, pp. 782–786, November 1966.
22. G. A. Thiele, "Wire Antennas," in *Computer Techniques for Electromagnetics*, R. Mittra (Ed.), Pergamon, New York, Chapter 2, pp. 7–70, 1973.
23. C. M. Butler and D. R. Wilton, "Evaluation of Potential Integral at Singularity of Exact Kernel in Thin-Wire Calculations," *IEEE Trans. Antennas Propagat.*, Vol. AP-23, No. 2, pp. 293–295, March 1975.
24. L. W. Pearson and C. M. Butler, "Inadequacies of Collocation Solutions to Pocklington-Type Models of Thin-Wire Structures," *IEEE Trans. Antennas Propagat.*, Vol. AP-23, No. 2, pp. 293–298, March 1975.
25. C. M. Butler and D. R. Wilton, "Analysis of Various Numerical Techniques Applied to Thin-Wire Scatterers," *IEEE Trans. Antennas Propagat.*, Vol. AP-23, No. 4, pp. 534–540, July 1975.
26. D. R. Wilton and C. M. Butler, "Efficient Numerical Techniques for Solving Pocklington's Equation and their Relationships to Other Methods," *IEEE Trans. Antennas Propagat.*, Vol. AP-24, No. 1, pp. 83–86, January 1976.
27. L. L. Tsai, "A Numerical Solution for the Near and Far Fields of an Annular Ring of Magnetic Current," *IEEE Trans. Antennas Propagat.*, Vol. AP-20, No. 5, pp. 569–576, September 1972.
28. R. Mittra and C. A. Klein, "Stability and Convergence of Moment Method Solutions," in *Numerical and Asymptotic Techniques in Electromagnetics*, R. Mittra (Ed.), Springer-Verlag, New York, 1975, Chapter 5, pp. 129–163.
29. T. K. Sarkar, "A Note on the Choice Weighting Functions in the Method of Moments," *IEEE Trans. Antennas Propagat.*, Vol. AP-33, No. 4, pp. 436–441, April 1985.
30. T. K. Sarkar, A. R. Djordjević and E. Arvas, "On the Choice of Expansion and Weighting

Functions in the Numerical Solution of Operator Equations," *IEEE Trans. Antennas Propagat.*, Vol. AP-33, No. 9, pp. 988–996, September 1985.
31. E. K. Miller and F. J. Deadrick, "Some Computational Aspects of Thin-Wire Modeling," in *Numerical and Asymptotic Techniques in Electromagnetics*, R. Mittra (Ed.), Springer-Verlag, New York, 1975, Chapter 4, pp. 89–127.
32. L. Kantorovich and G. Akilov, *Functional Analysis in Normed Spaces*, Pergamon, Oxford, pp. 586–587, 1964.
33. H. E. King, "Mutual Impedance of Unequal Length Antennas in Echelon," *IRE Trans. Antennas Propagat.*, Vol. AP-5, pp. 306–313, July 1957.
34. R. C. Hansen, "Fundamental Limitations in Antennas," *Proc. IEEE*, Vol. 69, No. 2, pp. 170–182, February 1981.
35. G. J. Burke and A. J. Poggio, "Numerical Electromagnetics Code (NEC)-method of moments," Technical Document 11, Naval Ocean Systems Center, San Diego, Calif., January 1981.
36. A. J. Julian, J. M. Logan, and J. W. Rockway, "MININEC: A Mini-Numerical Electromagnetics Code," Technical Document 516, Naval Ocean Systems Center, San Diego, Calif, September 6, 1982.
37. J. Rockway, J. Logan, D. Tam, and S. Li, *The MININEC SYSTEM: Microcomputer Analysis of Wire Antennas*, Artech House, 1988.
38. J. A. G. Malherbe, "Calculator Program for Mutual Impedance," *Microwave Journal*, (Euro-Global Ed.), pp. 82-H–82-M, February 1984.
39. J. A. G. Malherbe, "Analysis of a Linear Antenna Array Including the Effects of Mutual Coupling," *IEEE Trans. Education*, Vol. 32, No. 1, pp. 29–34, February 1989.
40. D. Rubin, *The Linville Method of High Frequency Transistor Amplifier Design*, Naval Weapons Center, NWCCL TP 845, Corona Labs., Corona, CA, March 1969.
41. J. L. Allen and B. L. Diamond, "Mutual Coupling in Array Antennas," Technical Report EDS-66-443, Lincoln Lab., MIT, October 4, 1966.
42. H. A. Wheeler, "The Radiation Resistance of an Antenna in an Infinite Array or Waveguide," *Proc. IRE*, Vol. 48, pp. 478–487, April 1948.
43. S. Edelberg and A. A. Oliner, "Mutual Coupling Effects in Large Antenna Arrays, Part I," *IRE Trans. Antennas Propagat.*, Vol. AP-8, No. 3, pp. 286–297, May 1960.
44. S. Edelberg and A. A. Olinder, "Mutual Coupling Effects in Large Antenna Arrays," Part II," *IRE Trans. Antennas Propagat.*, Vol. AP-8, No. 4, pp. 360–367, July 1960.
45. L. Stark, "Radiation Impedance of a Dipole in an Infinite Planar Phased Array," *Radio Science*, Vol. 3, pp. 361–375, 1966.
46. F. Zavosh and J. T. Aberle, "Infinite Phased Arrays of Cavity-Backed Patches," *IEEE Trans. Antennas Propagat.*, Vol. 42, No. 3, pp. 390–394, March 1994.
47. N. Amitay, V. Galindo, and C. P. Wu, *Theory and Analysis of Phased Array Antennas*, John Wiley and Sons, New York, 1972.
48. L. Stark, "Microwave Theory of Phased-Array Antennas—A Review," *Proc. IEEE*, Vol. 62, pp. 1661–1701, December 1974.
49. G. H. Knittel, A. Hessel and A. A. Oliner, "Element Pattern Nulls in Phased Arrays and Their Relation to Guided Waves," *Proc. IEEE*, Vol. 56, pp. 1822–1836, November 1968.
50. D. M. Pozar and D. H. Schaubert, "Scan Blindness in Infinite Phased Arrays of Printed Dipoles," *IEEE Trans. Antennas Propagat.*, Vol. AP-32, No. 6, pp. 602–610, June 1984.

PROBLEMS

8.1. Derive Pocklington's integral equation 8-24 using (8-22) and (8-23).
8.2. Derive the solution of (8-26) to the differential equation of (8-25a). Show that Hallén's integral equation can be written as (8-27).
8.3. Show that the incident tangential electric field (E_z^i) generated on the surface of a wire of radius a by a magnetic field generator of (8-30) is given by (8-31).
8.4. Reduce (8-31) to (8-32) valid only along the z axis ($\rho = 0$).

8.5. For the center-fed dipole of Example 8.3 write the [Z] matrix for $N = 21$ using for the gap the delta-gap generator and the magnetic-frill generator. Use the computer program MOMENT METHOD (POCKLINGTON) at the end of the chapter.

8.6. For an infinitesimal center-fed dipole of $\ell = \lambda/50$ of radius $a = 0.005\lambda$, derive the input impedance using Pocklington's integral equation with piecewise constant subdomain basis functions and point-matching. Use $N = 21$ and model the gap as a delta-gap generator and as a magnetic-frill generator. Use the MOMENT METHOD (POCKLINGTON) computer program at the end of the chapter.

8.7. Using the MOMENT METHOD (HALLÉN) computer program at the end of the chapter, compute the input impedance of a $\lambda/4$ and $3\lambda/4$ dipole with an l/d ratio of $l/d = 50$ and 25. Use 20 subsections. Compare the results with the impedances of a dipole with $l/d = 10^9$. Plot the current distribution and the far-field pattern of each dipole.

8.8. Derive (8-53)–(8-55b) using (8-52), (3-2a), and (4-56).

8.9. For a linear dipole with sinusoidal current distribution, radiating in free-space, find the radiation Z_{tm} and the input Z_{in} impedances when $a = \lambda/20$. Verify using the computer program SELF AND MUTUAL IMPEDANCES at the end of the chapter.
(a) $l = \lambda/4$ (b) $l = \lambda/2$
(c) $l = 3\lambda/4$ (d) $l = \lambda$

8.10. A $\lambda/2$ dipole of finite radius is not self-resonant. However, if the dipole is somewhat less than $\lambda/2$, it becomes self-resonant. For a dipole with radius of $a = \lambda/200$ radiating in free-space, find the
(a) *nearest length by which the $\lambda/2$ dipole becomes self-resonant*
(b) radiation resistance (referred to the current maximum) of the new resonant dipole
(c) input resistance
(d) VSWR when the dipole is connected to a 50-ohm line

8.11. Find the length, at the first resonance, of linear dipoles with wire radii of
(a) $10^{-5}\lambda$ (b) $10^{-4}\lambda$
(c) $10^{-3}\lambda$ (d) $10^{-2}\lambda$
Compute the radiation resistance of each.

8.12. A quarter-wavelength monopole of radius $a = 10^{-2}\lambda$ is placed upon an infinite ground plane. Determine the
(a) impedance of the monopole
(b) *length by which it must be shortened to become self-resonant (first resonance)*
(c) impedance of the monopole when its length is that given in part b.
(d) VSWR when the monopole of part b is connected to a 50-ohm line.

8.13. For two half-wavelength dipoles radiating in free-space, compute (using equations, *not* curves) the mutual impedance Z_{21_m} referred to the current maximum for
(a) side-by-side arrangement with $d = \lambda/4$
(b) collinear configuration with $s = \lambda/4$
Verify using the computer program SELF AND MUTUAL IMPEDANCES at the end of the chapter.

8.14. Two identical linear $\lambda/2$ dipoles are placed in a collinear arrangement a distance $s = 0.35\lambda$ apart. Find the driving point impedance of each. Verify using the computer *program SELF AND MUTUAL IMPEDANCES at the end of the chapter.*

8.15. Two identical linear $\lambda/2$ dipoles are placed in a collinear arrangement. Find the spacings between them so that the driving point impedance of each has the smallest reactive part.

```
C*****************************************************************
C
C THIS IS A FORTRAN MOMENT METHOD PROGRAM USING
C
C     I.  POCKLINGTON'S [Equ. (8-24)]
C     II. HALLEN'S [Equ. (8-27)]
C
C INTEGRAL EQUATIONS TO COMPUTE THE:
C
C     A. CURRENT DISTRIBUTION
C     B. INPUT IMPEDANCE
C     C. NORMALIZED AMPLITUDE RADIATION PATTERN
C
C OF A LINEAR SYMMETRICALLY EXCITED DIPOLE.
C
C THIS PROGRAM USES PULSE EXPANSION FOR THE ELECTRIC
C CURRENT MODE AND POINT-MATCHING THE ELECTRIC
C FIELD AT THE CENTER OF EACH WIRE SEGMENT
C
C DELTA-GAP FEED MODEL IS USED IN BOTH FORMULATIONS.
C IN ADDITION, MAGNETIC-FRILL GENERATOR IS AVAILABLE IN
C THE POCKLINGTON'S INTEGRAL EQUATION
C
C
C     OPTION I.  POCKLINGTON'S INTEGRAL EQUATION
C     OPTION II. HALLEN'S INTEGRAL EQUATION
C
C          **INPUT PARAMETERS
C          1. TL  =  TOTAL LENGTH OF THE DIPOLE (in wavelengths)
C          2. RA  =  RADIUS OF THE WIRE (in wavelengths)
C          3. NM  =  TOTAL NUMBER OF SUBSECTIONS
C                    (must be an odd integer)
C          4. IEX =  OPTION TO USE EITHER MAGNETIC-FRILL
C                    GENERATOR OR DELTA-GAP FEED
C             IEX =  1: MAGNETIC-FRILL GENERATOR
C             IEX =  2: DELTA-GAP FEED
C
C          **NOTE
C          IGNORE INPUT PARAMETER IEX WHEN CHOOSING OPTION II
C          (i.e., HALLEN'S FORMULATION)
C
C*****************************************************************
```

COMPUTER PROGRAM - SELF AND MUTUAL IMPEDANCES

```
C**********************************************************************
C
C THIS IS A FORTRAN PROGRAM THAT COMPUTES THE:
C
C     I.  SELF IMPEDANCE FOR ANY LENGTH DIPOLE
C     II. MUTUAL IMPEDANCE BETWEEN TWO IDENTICAL
C         LINEAR DIPOLES
C
C BASED ON THE INDUCED EMF METHOD AND THE IDEAL CURRENT
C DISTRIBUTION OF EQUATION (4-56)
C
C THE IMPEDANCES CAN BE COMPUTED BASED EITHER ON THE CURRENT
C AT THE INPUT, OR ON THE CURRENT MAXIMUM:
C
C     I. SELF IMPEDANCE (INPUT IMPEDANCE)
C
C          1. BASED ON CURRENT AT THE INPUT:
C               Zin  = Rin + j Xin
C               Rin  = INPUT RESISTANCE [Equs.(8-60a) and (8-61a)]
C               Xin  = INPUT REACTANCE [Equs.(8-60b) and (8-61b)]
C
C          2. BASED ON CURRENT MAXIMUM:
C               Zinm = Rinm + j Xinm
C               Rinm = SELF RESISTANCE [Equ. (8-60a)]
C               Xinm = SELF REACTANCE [Equ. (8-60b)]
C
C     II. MUTUAL IMPEDANCE
C
C          1. BASED ON CURRENT AT THE INPUT:
C               Z21i = R21i + j X21i [Equ. (8-68)]
C               R21i = MUTUAL RESISTANCE
C               X21i = MUTUAL REACTANCE
C
C          2. BASED ON CURRENT MAXIMUM:
C               Z21m = R21m + j X21m [Equ. (8-70)]
C               R21m = MUTUAL RESISTANCE
C               X21m = MUTUAL REACTANCE
C
C THE DIPOLES FOR MUTUAL IMPEDANCE COMPUTATIONS MUST BE
C IDENTICAL WITH LENGTH OF ODD MULTIPLES OF λ/2
C (l = nλ/2, n = 1,3,5,..).
C
C
C     OPTION I.  SELF IMPEDANCE (INPUT IMPEDANCE)
C
C          **ARRAY INPUT PARAMETERS
C          1. l  = LENGTH OF THE DIPOLE
C          2. a  = RADIUS OF THE DIPOLE
C
C                                                  (continued on next page)
```

```
C                                                                    (continued)
C
C
C     OPTION II.  MUTUAL IMPEDANCE
C
C       CHOICE A: SIDE-BY-SIDE [see Fig. 8.19(a)]
C
C          **ARRAY INPUT PARAMETERS
C          1. l  = LENGTH OF THE DIPOLES
C          2. d  = HORIZONTAL DISPLACEMENT OF DIPOLES
C
C       CHOICE B: COLLINEAR [see Fig. 8.19(b)]
C
C          **ARRAY INPUT PARAMETERS
C          1. l  = LENGTH OF THE DIPOLES
C          2. h  = VERTICAL DISPLACEMENT OF DIPOLES
C
C       CHOICE C: PARALLEL-IN-ECHELON [see Fig. 8.19(c)]
C
C          **ARRAY INPUT PARAMETERS
C          1. l  = LENGTH OF THE DIPOLE
C          2. h  = VERTICAL DISPLACEMENT OF DIPOLES
C          2. d  = HORIZONTAL DISPLACEMENT OF DIPOLES
C
C
C       **NOTE
C       ALL THE INPUT DATA ARE IN WAVELENGTHS.
C
C**********************************************************************
```